

ИНСТИТУТ ЗА ФИЗИКУ

ПРИМЉЕНО:		29. 12. 2021	
Рад.јед.	б р о ј	Арх.шифра	Прилог
0801	1285/1		

Научном већу Института за физику

Београд, 29. 12. 2021.

Предмет: Покретање поступка у звање истраживач сарадник

Молим Научно веће Института за физику у Београду да покрене поступак за мој избор у звање **Истраживач сарадник**, имајући у виду да испуњавам све критеријуме прописане од стране Министарства просвете, науке и технолошког развоја Републике Србије за стицање наведеног звања.

У прилогу достављам:

1. мишљење руководиоца пројекта са предлогом комисије за избор у звање;
2. стручну биографију;
3. преглед научне активности;
4. списак и копије објављених научних радова и других публикација;
5. уверење о последњем овереном и уписаном семестру на докторским студијама;
6. фотокопију диплома са основних и мастер студија;
7. потврду о прихватању теме докторске дисертације.

С поштовањем,



Стефан Стојку,
истраживач приправник

9. децембар 2021

Научном већу Института за физику

Предмет: Мишљење руководиоца лабораторије за избор Стефана Стојкуа у звање истраживач сарадник

Поштовани,

Стефан Стојку завршио је основне, а потом и мастер студије на Физичком факултету Универзитета у Београду. Мастер тезу одбранио је у јулу 2019. године. Докторске студије на смеру Физика високих енергија и нуклеарна физика на Физичком факултету Универзитета у Београду уписао је 2019. године. Положио је све предвиђене испите. Тема његове докторске дисертације представљена је и прихваћена на Колегијуму докторских студија Физичког факултета Универзитета у Београду 1. децембра 2021. године. Ангажован је у групи др Магдалене Ђорђевић и бави се истраживањем кварк-глуонске плазме.

С обзиром да Стефан Стојку испуњава све услове предвиђене Правилником о поступку и начину вредновања, и квантитативном исказивању научноистраживачких резултата истраживача, сагласна сам са покретањем поступка за избор у звање истраживач сарадник.

За чланове комисије за избор Стефана Стојкуа у звање истраживач сарадник предлажем следећи састав:

1. др Магдалена Ђорђевић, научни саветник, Институт за физику;
2. др Игор Салом, виши научни сарадник, Институт за физику;
3. проф. др Воја Радовановић, редовни професор Физичког факултета;

Руководилац лабораторије за физику високих енергија,



др Лидија Живковић
Научни саветник

Биографија Стојку Стефана

Стефан Стојку је рођен 15. 04. 1994. године у Панчеву, где је завршио гимназију „Урош Предић”. Основне студије уписао је 2012. године на Физичком факултету, смер Теоријска и експериментална физика и дипломирао 2018. године са просечном оценом 9,82. Мастер студије, уписане 2018. године на Физичком факултету, завршава 2019. године са просечном оценом 9,67. Мастер тезу под називом „Одређивање фактора пропорционалности температурске зависности губитака енергије у кварк-глуонској плазми из експерименталних података” израђује под менторством др Магдалене Ђорђевић у оквиру Лабораторије за физику високих енергија Института за физику у Београду и брани у јулу 2019. године.

2019. године на Физичком факултету Универзитета у Београду уписује докторске студије у области истраживања релативистичких судара тешких јона и кварк-глуонске плазме. Истраживање ради под менторством др Магдалене Ђорђевић. Био је ангажован на пројекту основних истраживања Министарства просвете, науке и технолошког развоја Републике Србије ОИ 171004 („ATLAS експеримент и физика честица на *LHC* енергијама”) у Лабораторији за физику високих енергија Института за физику у Београду. Ангажован је и на пројекту Horizon 2020 ERC-2016-CoG:725741 (“A novel Quark-Gluon Plasma tomography tool: from jet quenching to exploring the extreme medium properties”). Тему докторске дисертације под називом: „Проучавање особина кварк-глуонске плазме помоћу високоенергијских честица” успешно брани пред Колегијумом докторских студија 1. 12. 2021.

Стефан Стојку започео је рад на Институту за физику 01. 10. 2018. године по основу ангажовања на горе наведеном ERC пројекту чији је руководиоца др Магдалена Ђорђевић. 5. 11. 2019. године добија звање Истраживач приправник и од 18. 12. 2019. године запослен је на Институту за физику.

До сада је објавио 3 научна рада у области теоријске нуклеарне физике од којих је наведен као први аутор на једном раду. Такође, коаутор је на једном раду у области квантитативне биологије. Истраживање које се спроводи у оквиру пројеката на којима је ангажован представио је на међународним конференцијама и радионицама из области кварк-глуонске плазме, од којих су неке: Strangeness in Quark Matter 2019, Zimanyi School 2019, Initial Stages 2020, Online Strangeness in Quark Matter 2020... Учествовао је и на четири школе.

Говори српски, енглески, румунски и немачки језик.

Преглед научне активности Стефана Стојку

Истраживање Стефана Стојку је у области теоријског проучавања кварк-глуонске плазме. Циљ истраживања је примена претходно развијеног DREENA модела за проучавање особина кварк-глуонске плазме, као и побољшање DREENA модела. У свом досадашњем раду, радио је на одређивању зависности губитака енергије високоенергијских честица у КГП од температуре, а радио је и на развоју методе за одређивање просторне анизотропије кварк-глуонске плазме из високоенергијских података. Осим тога, ради на проучавању раних стадијума еволуције кварк-глуонске плазме.

Резултати везани за одређивање температурске зависности губитака енергије високоенергијских честица у КГП чине део његовог мастер рада, а објављени су у Phys. Rev. C **103**, 024908 раду, на којем је Стефан Стојку први аутор. У овом раду је помоћу аналитичких аргумената утврђено коју опсерваблу је могуће употребити за одређивање ове температурске зависности. Затим су вредности ове опсервабле израчунате у оквиру DREENA-C модела, и одређено је да је зависност губитака енергије високоенергијских честица од температуре скоро линеарна, што је у супротности са другим (једноставнијим) моделима, и у складу са мноштвом експерименталних података.

Досадашњи резултати везани за проучавање анизотропије КГП су објављени у Phys. Rev. C **100**, 031901(R) раду. У овом раду је испитано да ли и на који начин је могуће довести у везу високоенергијске податке са просторном анизотропијом кварк-глуонске плазме. Помоћу једноставних закона скалирања и аналитичких аргумената који су оправдани у оквиру нашег модела, закључено за коју високоенергијску опсерваблу се очекује да је у вези са просторном анизотропијом кварк-глуонске плазме. Потом је ова опсервабла израчуната у оквиру DREENA-B модела, где се медијум моделује као једноставна 1+1D лонгитудинална експанзија (без трансверзалне експанзије). Из добијених резултата је екстрахована вредност параметра који описује просторну анизотропију кварк-глуонске плазме. Добијене вредности су упоређене са стандардним вредностима за просторну анизотропију из литературе, и опажа се добро слагање. Даље истраживање ће се наставити коришћењем DREENA-A модела, где се медијум моделује као 3+1D хидродинамичка еволуција. Опсервабла за коју је у оквиру DREENA-B модела добијено да се може довести у везу са просторном анизотропијом ће бити израчуната у оквиру овог модела, а затим ће се испитати да ли и на који начин описује анизотропију медијума.

Стефан Стојку истраживање наставља у смеру проучавања раних стадијума еволуције кварк-глуонске плазме, односно, еволуције пре времена термализације. У првој фази овог истраживања је испитано време термализације кварк-глуонске плазме. Ово је изведено тако што је генерисано више температурских профила са различитим временима термализације, а затим су у оквиру DREENA-A модела на овим профилима израчунате високоенергијске опсервабле, које су затим упоређене са експерименталним подацима. Закључено је да касније време термализације даје боље слагање са експерименталним подацима. Даље истраживање иде у смеру имплементације нетривијалне еволуције КГП пре термализације.

Искуство из нумеричке анализе података је применио у квантитативној биологији, на једном од тренутно најакутелнијих проблема – разумевању динамике преношења COVID-19 у популацији. Резултати овог истраживања су објављени у Global Challenges 2021, 5, 2000101 раду.

Листа М20 публикација

А. Теоријска нуклеарна физика

1. Magdalena Djordjevic, Stefan Stojku, Dusan Zigic, Bojana Ilic, Jussi Auvinen, Igor Salom, Marko Djordjevic and Pasi Huovinen, *From high p_{\perp} theory and data to inferring anisotropy of Quark-Gluon Plasma*, Nucl. Phys. A 1005, 121900 (2021) (M22, IF 1.695)
2. Stefan Stojku, Bojana Ilic, Marko Djordjevic, and Magdalena Djordjevic, *Extracting the temperature dependence in high- p_{\perp} particle energy loss*, Phys. Rev. C **103**, 024908 (M21, IF 3.82)
3. Magdalena Djordjevic, Stefan Stojku, Marko Djordjevic, and Pasi Huovinen, *Shape of the quark gluon plasma droplet reflected in the high- p_{\perp} data*, Phys. Rev. C **100**, 031901(R) (M21, IF 3.82)

Б. Квантитативна биологија

1. Magdalena Djordjevic, Marko Djordjevic, Bojana Ilic, Stefan Stojku, Igor Salom, *Understanding Infection Progression under Strong Control Measures through Universal COVID-19 Growth Signatures. Global Challenges* 2021, 5, 2000101 (M21, IF 4.306)

Саопштења са међународног скупа штампана у изводу (категорија М34)

Напомена: испод су укључена само саопштења која је кандидат сам излагао, не и саопштења коаутора.

А. Предавања

1. Stefan Stojku, Marko Djordjevic, Pasi Huovinen, Magdalena Djordjevic, *Shape of the quark-gluon plasma droplet reflected in the high- p_{\perp} data*, Zimanyi school 2019: 19th Zimanyi school - Winter workshop on heavy ion physics, December 2019, Budapest, Hungary
2. Stefan Stojku, Marko Djordjevic, Pasi Huovinen, Magdalena Djordjevic, *From high- p_{\perp} theory and data to inferring the anisotropy of quark-gluon plasma*, Frontiers in Nuclear and Hadronic Physics 2020, Florence, Italy
3. Stefan Stojku, Jussi Auvinen, Marko Djordjevic, Pasi Huovinen, Magdalena Djordjevic, *QGP tomography: inferring bulk medium properties from high- p_{\perp} data*, Zimanyi school 2020: 20th Zimanyi school - Winter workshop on heavy ion physics, December 2020, Budapest, Hungary
4. Stefan Stojku, Jussi Auvinen, Marko Djordjevic, Pasi Huovinen, Magdalena Djordjevic, *Thermalization time constrained by high- p_{\perp} QGP tomography*, Online Strangeness in Quark Matter Conference 2021, May 2021
5. Stefan Stojku, Jussi Auvinen, Marko Djordjevic, Pasi Huovinen, Magdalena Djordjevic, *Anisotropy of quark-gluon plasma inferred from high- p_{\perp} data*, Workshop of the Network NA7-Hf-QGP of the European program 'STRONG-2020' and the HFHF, October 2021, Hersonissos, Crete, Greece

Б. Постери

1. Stefan Stojku, Magdalena Djordjevic, *From R_{AA} to energy loss temperature proportionality factor*, Strangeness in Quark Matter, Jun 2019, Bari, Italy
2. Stefan Stojku, Jussi Auvinen, Marko Djordjevic, Pasi Huovinen, Magdalena Djordjevic, *QGP tomography: inferring bulk medium properties from high- p_{\perp} data*, Initial Stages 2021, January 2021, Weizmann Institute of Science, Israel

Shape of the quark gluon plasma droplet reflected in the high- p_{\perp} data

Magdalena Djordjevic,^{1,*} Stefan Stojku,¹ Marko Djordjevic,² and Pasi Huovinen¹

¹*Institute of Physics Belgrade, University of Belgrade, Serbia*

²*Faculty of Biology, University of Belgrade, Serbia*



(Received 19 April 2019; revised manuscript received 1 August 2019; published 12 September 2019)

We show, through analytic arguments, numerical calculations, and comparison with experimental data, that the ratio of the high- p_{\perp} observables $v_2/(1 - R_{AA})$ reaches a well-defined saturation value at high p_{\perp} , and that this ratio depends only on the spatial anisotropy of the quark gluon plasma (QGP) formed in ultrarelativistic heavy-ion collisions. With expected future reduction of experimental errors, the anisotropy extracted from experimental data will further constrain the calculations of initial particle production in heavy-ion collisions and thus test our understanding of QGP physics.

DOI: [10.1103/PhysRevC.100.031901](https://doi.org/10.1103/PhysRevC.100.031901)

Introduction. The major goal of relativistic heavy-ion physics [1–4] is understanding the properties of the new form of matter called quark gluon plasma (QGP) [5,6], which, in turn, allows the understanding of properties of QCD matter at its most basic level. Energy loss of rare high-momentum partons traversing this matter is known to be an excellent probe of its properties. Different observables such as the nuclear modification factor R_{AA} and the elliptic flow parameter v_2 of high- p_{\perp} particles, probe the medium in different manners, but they all depend not only on the properties of the medium, but also on the density, size, and shape of the QGP droplet created in a heavy-ion collision. Thus drawing firm conclusions of the material properties of QGP is very time consuming and requires simultaneous description of several observables. It would therefore be very useful if there were an observable, or combination of observables, which would be sensitive to only one or just a few of all the parameters describing the system.

For high- p_{\perp} particles, spatial asymmetry leads to different paths, and consequently to different energy losses. Consequently, v_2 (angular differential suppression) carries information on both the spatial anisotropy and material properties that affect energy loss along a given path. On the other hand, R_{AA} (angular average suppression) carries information only on material properties affecting the energy loss [7–10], so one might expect to extract information on the system anisotropy by taking a ratio of expressions which depend on v_2 and R_{AA} . Of course, it is far from trivial whether such intuitive expectations hold, and what combination of v_2 and R_{AA} one should take to extract the spatial anisotropy. To address this, we here use both analytical and numerical analysis to show

that the ratio of v_2 and $1 - R_{AA}$ at high p_{\perp} depends only on the spatial anisotropy of the system. This approach provides a complementary method for evaluating the anisotropy of the QGP fireball, and advances the applicability of high- p_{\perp} data to a new level as, up to now, these data were mainly used to study the jet-medium interactions, rather than inferring bulk QGP parameters.

Anisotropy and high- p_{\perp} observables. In [10,11], we showed that at very large values of transverse momentum p_{\perp} , the fractional energy loss $\Delta E/E$ (which is very complex, both analytically and numerically, due to inclusion of multiple effects, see *Numerical results* for more details) shows asymptotic scaling behavior

$$\Delta E/E \approx \chi(p_{\perp}) \langle T \rangle^a \langle L \rangle^b, \quad (1)$$

where $\langle L \rangle$ is the average path length traversed by the jet, $\langle T \rangle$ is the average temperature along the path of the jet, χ is a proportionality factor (which depends on initial jet p_{\perp}), and a and b are proportionality factors which determine the temperature and path-length dependence of the energy loss. Based on Refs. [12–15], we might expect values like $a = 3$ and $b = 1$ or 2, but a fit to a full-fledged calculation yields values $a \approx 1.2$ and $b \approx 1.4$ [11,16]. Thus the temperature dependence of the energy loss is close to linear, while the length dependence is between linear and quadratic. To evaluate the path length we follow Ref. [17]:

$$L(x, y, \phi) = \frac{\int_0^{\infty} d\lambda \lambda \rho(x + \lambda \cos(\phi), y + \lambda \sin(\phi))}{\int_0^{\infty} d\lambda \rho(x + \lambda \cos(\phi), y + \lambda \sin(\phi))}, \quad (2)$$

which gives the path length of a jet produced at point (x, y) heading to direction ϕ , and where $\rho(x, y)$ is the initial density distribution of the QGP droplet. To evaluate the average path length we take average over all directions and production points.

If $\Delta E/E$ is small (i.e., for high p_{\perp} and in peripheral collisions), we obtain [7,10,11]

$$R_{AA} \approx 1 - \xi \langle T \rangle^a \langle L \rangle^b, \quad (3)$$

*magda@ipb.ac.rs

Published by the American Physical Society under the terms of the [Creative Commons Attribution 4.0 International](https://creativecommons.org/licenses/by/4.0/) license. Further distribution of this work must maintain attribution to the author(s) and the published article's title, journal citation, and DOI. Funded by SCOAP³.

where $\xi = (n-2)\chi/2$, and n is the steepness of a power-law fit to the transverse momentum distribution, $dN/dp_\perp \propto 1/p_\perp^n$. Thus $1 - R_{AA}$ is proportional to the average size and temperature of the medium. To evaluate the anisotropy we define the average path lengths in the in-plane and out-of-plane directions,

$$\begin{aligned} \langle L_{in} \rangle &= \frac{1}{\Delta\phi} \int_{-\Delta\phi/2}^{\Delta\phi/2} d\phi \langle L(\phi) \rangle, \\ \langle L_{out} \rangle &= \frac{1}{\Delta\phi} \int_{\pi/2-\Delta\phi/2}^{\pi/2+\Delta\phi/2} d\phi \langle L(\phi) \rangle, \end{aligned} \quad (4)$$

where $\Delta\phi = \pi/6$ [18] is the acceptance angle with respect to the event plane (in-plane) or orthogonal to it (out-of-plane), and $\langle L(\phi) \rangle$ the average path length in the ϕ direction. Note that the obtained calculations are robust with respect to the precise value of the small angle $\pm\Delta\phi/2$, but we still keep a small cone ($\pm\pi/12$) for R_{AA}^{in} and R_{AA}^{out} calculations, to have the same numerical setup as in our Ref. [10]. Now we can write $\langle L \rangle = (\langle L_{out} \rangle + \langle L_{in} \rangle)/2$ and $\Delta L = (\langle L_{out} \rangle - \langle L_{in} \rangle)/2$. Similarly, the average temperature along the path length can be split to average temperatures along paths in in- and out-of-plane directions, $\langle T_{in} \rangle = \langle T \rangle + \Delta T$ and $\langle T_{out} \rangle = \langle T \rangle - \Delta T$. When applied to an approximate way to calculate v_2 of high- p_\perp particles [19], we obtain¹

$$\begin{aligned} v_2 &\approx \frac{1}{2} \frac{R_{AA}^{in} - R_{AA}^{out}}{R_{AA}^{in} + R_{AA}^{out}} \approx \frac{\xi \langle T_{out} \rangle^a \langle L_{out} \rangle^b - \xi \langle T_{in} \rangle^a \langle L_{in} \rangle^b}{4} \\ &\approx \xi \langle T \rangle^a \langle L \rangle^b \left(\frac{b}{2} \frac{\Delta L}{\langle L \rangle} - \frac{a}{2} \frac{\Delta T}{\langle T \rangle} \right), \end{aligned} \quad (5)$$

where we have assumed that $\xi \langle T \rangle^a \langle L \rangle^b \ll 1$, and that $\Delta L/\langle L \rangle$ and $\Delta T/\langle T \rangle$ are small as well.

By combining Eqs. (3) and (5), we obtain

$$\frac{v_2}{1 - R_{AA}} \approx \left(\frac{b}{2} \frac{\Delta L}{\langle L \rangle} - \frac{a}{2} \frac{\Delta T}{\langle T \rangle} \right). \quad (6)$$

This ratio carries information on the anisotropy of the system, but through both spatial ($\Delta L/\langle L \rangle$) and temperature ($\Delta T/\langle T \rangle$) variables. From Eq. (6), we see the usefulness of the (approximate) analytical derivations, since the term $(1 - R_{AA})$ in the denominator could hardly have been deduced intuitively or pinpointed by numerical trial and error. Figure 1 shows a linear dependence $\Delta L/\langle L \rangle \approx c \Delta T/\langle T \rangle$, where $c \approx 4.3$, with the temperature evolution given by one-dimensional (1D) Bjorken expansion, as sufficient to describe the early evolution of the system. Equation (6) can thus be simplified to

$$\begin{aligned} \frac{v_2}{1 - R_{AA}} &\approx \frac{1}{2} \left(b - \frac{a}{c} \right) \frac{\langle L_{out} \rangle - \langle L_{in} \rangle}{\langle L_{out} \rangle + \langle L_{in} \rangle} \approx 0.57\zeta, \\ \text{where } \zeta &= \frac{\langle L_{out} \rangle - \langle L_{in} \rangle}{\langle L_{out} \rangle + \langle L_{in} \rangle} \quad \text{and} \quad \frac{1}{2} \left(b - \frac{a}{c} \right) \approx 0.57, \end{aligned} \quad (7)$$

¹Note that the first approximate equality in Eq. (5) can be shown to be exact if the higher harmonics v_4, v_6 , etc., are zero, and the opening angle where R_{AA}^{in} and R_{AA}^{out} are evaluated is zero [cf. definitions of $\langle L_{out} \rangle$ and $\langle L_{in} \rangle$, Eq. (4)].

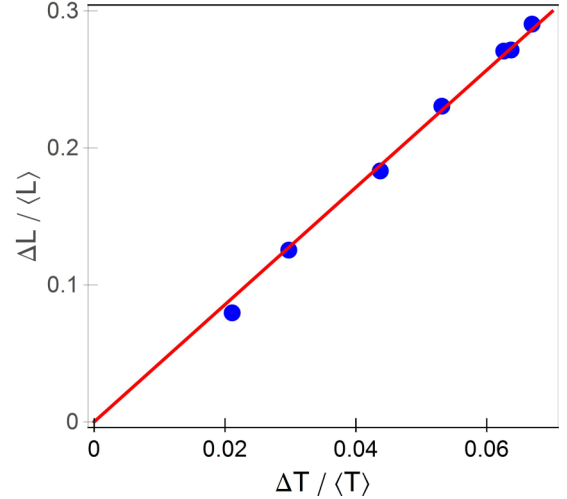


FIG. 1. $\Delta T/\langle T \rangle$ vs $\Delta L/\langle L \rangle$ in Pb+Pb collisions at $\sqrt{s_{NN}} = 5.02$ TeV collision energy at various centralities [7,10]. The more peripheral the collision, the larger the values. The red solid line depicts linear fit to the values.

when $a \approx 1.2$ and $b \approx 1.4$. Consequently, the asymptotic behavior of observables R_{AA} and v_2 is such that at high p_\perp , their ratio is dictated solely by the geometry of the fireball. Therefore, the anisotropy parameter ζ can be extracted from the high- p_\perp experimental data.

Regarding the parametrization used to derive Eq. (7) (constants a , b , and c), we note that a and b are well established within our dynamical energy-loss formalism and follow from R_{AA} predictions that are extensively tested on experimental data [11,16] and do not depend on the details of the medium evolution. Regarding c , it may (to some extent) depend on the type of implemented medium evolution, but this will not affect the obtained scaling, only (to some extent) the overall prefactor in Eq. (7).

Numerical results. To assess the applicability of the analytically derived scaling in Eq. (7), we calculate $v_2/(1 - R_{AA})$ using our full-fledged numerical procedure for calculating the fractional energy loss. This procedure is based on our state-of-the-art dynamical energy-loss formalism [20,21], which has several unique features in the description of high- p_\perp parton medium interactions: (i) The formalism takes into account a *finite-size, finite-temperature* QCD medium consisting of *dynamical* (that is, moving) partons, contrary to the widely used static scattering approximation and/or medium models with vacuum-like propagators (e.g., [12–15]). (ii) The calculations are based on the finite-temperature generalized hard-thermal-loop approach [22], in which the infrared divergences are naturally regulated [20,21,23]. (iii) Both radiative [20] and collisional [21] energy losses are calculated under *the same* theoretical framework, applicable to both light and heavy flavor. (iv) The formalism is generalized to the case of finite magnetic [24] mass and running coupling [25] and towards removing the widely used soft-gluon approximation [26]. The formalism was further embedded into our recently developed DREENA-B framework [10], which integrates initial momentum distribution of leading partons [27], energy

loss with path-length [17] and multigluon [28] fluctuations and fragmentation functions [29], in order to generate the final medium modified distribution of high- p_{\perp} hadrons. The framework was recently used to obtain joint R_{AA} and v_2 predictions for 5.02 TeV Pb+Pb collisions at the LHC [10], showing a good agreement with the experimental data.

We have previously shown [30] that all the model ingredients noted above have an effect on the high- p_{\perp} data, and thus should be included to accurately explain it. In that respect, our model is different from many other approaches, which use a sophisticated medium evolution, but an (over)simplified energy-loss model. Our previous work, however, shows that for explaining the high- p_{\perp} data, an accurate description of high- p_{\perp} parton-medium interactions is at least as important as an advanced medium evolution model. For example, the dynamical energy-loss formalism, embedded in 1D Bjorken expansion, explains well the v_2 puzzle [10], i.e., the inability of other models to jointly explain R_{AA} and v_2 measurements. To what extent the dynamical energy-loss predictions will change when embedded in full three-dimensional evolution is at the time of this writing still unknown, but our previous results nevertheless make it plausible that calculations employing simple one-dimensional expansion can provide valuable insight into the behavior of jets in the medium.

Our results for the longitudinally expanding system (1D Bjorken) and the corresponding data are shown in Fig. 2. The gray band shows our full DREENA-B result (see above) with the band resulting from the uncertainty in the magnetic to electric mass ratio μ_M/μ_E [31,32]. The red line corresponds to the 0.57ζ limit from Eq. (7), where ζ is the anisotropy of the path lengths used in the DREENA-B calculations [7,10]. Importantly, for each centrality, the asymptotic regime—where the $v_2/(1 - R_{AA})$ ratio does not depend on p_{\perp} , but is determined by the geometry of the system—is already reached from $p_{\perp} \approx 20\text{--}30$ GeV; the asymptote corresponds to the analytically derived Eq. (7), within $\pm 5\%$ accuracy. It is also worth noticing that our prediction of asymptotic behavior was based on approximations which are not necessarily valid in these calculations, but the asymptotic regime is nevertheless reached, telling us that those assumptions were sufficient to capture the dominant features. If, as we suspect, the high- p_{\perp} parton-medium interactions are more important than the medium evolution model in explaining the high- p_{\perp} data, this behavior reflects this importance and the analytical derivations based on a static medium may capture the dominant features seen in Fig. 2.

Furthermore, to check if the experimental data support the derived scaling relation, we compare our results to the ALICE [33,34], CMS [35,36], and ATLAS [37,38] data for $\sqrt{s_{NN}} = 5.02$ TeV Pb+Pb collisions. The experimental data, for all three experiments, show the same tendency, i.e., the independence on the p_{\perp} and a consistency with our predictions, though the error bars are still large. Therefore, from Fig. 2, we see that at each centrality both the numerically predicted and experimentally observed $v_2/(1 - R_{AA})$ approach the same high- p_{\perp} limit. This robust, straight line, asymptotic value carries information about the system's anisotropy, which is, in principle, simple to infer from the experimental data.

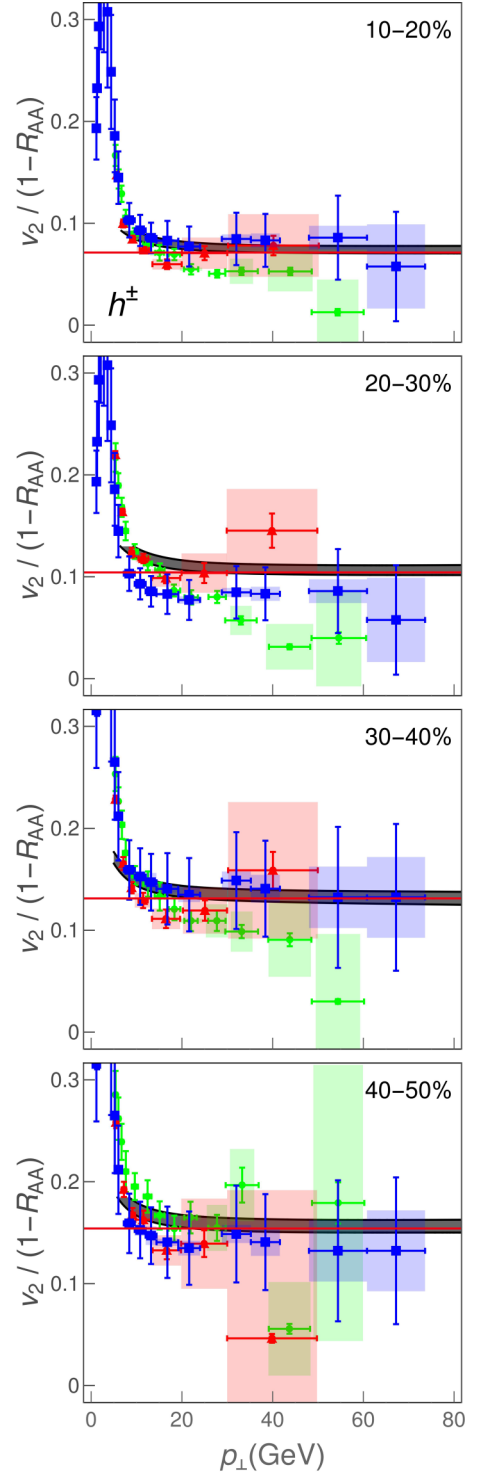


FIG. 2. Theoretical predictions for $v_2/(1 - R_{AA})$ ratio of charged hadrons as a function of transverse momentum p_{\perp} compared with 5.02 TeV Pb+Pb ALICE [33,34] (red triangles), CMS [35,36] (blue squares), and ATLAS [37,38] (green circles) data. Panels correspond to 10–20%, 20–30%, 30–40%, and 40–50% centrality bins. The gray band corresponds to the uncertainty in the magnetic to electric mass ratio μ_M/μ_E . The upper (lower) boundary of the band corresponds to $\mu_M/\mu_E = 0.4$ (0.6) [31,32]. In each panel, the red line corresponds to the limit 0.57ζ from Eq. (7).

Ideally, the experimental data (here from ALICE, CMS, and ATLAS) would overlap with each other, and would moreover have small error bars. In such a case, the data could be used to directly extract the anisotropy parameter ζ by fitting a straight line to the high- p_\perp part of the $v_2/(1 - R_{AA})$ ratio. While such direct anisotropy extraction would be highly desirable, the available experimental data are unfortunately still not near the precision level needed to implement this. However, we expect this to change in the upcoming high-luminosity third run at the LHC, where the error bars are expected to be significantly reduced, so that this procedure can be directly applied to experimental data.

It is worth remembering that the anisotropy parameter ζ , which can be extracted from the high- p_\perp data, is not the commonly used anisotropy parameter ϵ_2 ,

$$\epsilon_2 = \frac{\langle y^2 - x^2 \rangle}{\langle y^2 + x^2 \rangle} = \frac{\int dx dy (y^2 - x^2) \rho(x, y)}{\int dx dy (y^2 + x^2) \rho(x, y)}, \quad (8)$$

where $\rho(x, y)$ is the initial density distribution of the QGP droplet. We may also expect, that once the transverse expansion is included in the description of the evolution, the path-length anisotropy ζ reflects the time-averaged anisotropy of the system, and therefore is not directly related to the initial-state anisotropy ϵ_2 . Nevertheless, it is instructive to check how the path-length anisotropy in our simple model relates to conventional ϵ_2 values in the literature. For this purpose we construct a variable

$$\epsilon_{2L} = \frac{\langle L_{\text{out}} \rangle^2 - \langle L_{\text{in}} \rangle^2}{\langle L_{\text{out}} \rangle^2 + \langle L_{\text{in}} \rangle^2} = \frac{2\zeta}{1 + \zeta^2}. \quad (9)$$

We have checked that for different density distributions ϵ_2 and ϵ_{2L} agree within $\approx 10\%$ accuracy.

We have extracted the parameters ζ from the DREENA-B results shown in Fig. 2; the corresponding ϵ_{2L} results are shown as a function of centrality in Fig. 3 and compared to ϵ_2 evaluated using various initial-state models in the literature [39–42]. Note that conventional (EKRT [40], IP-Glasma [41]) ϵ_2 values trivially agree with our *initial* ϵ_2 (not shown in the figure), i.e., the initial ϵ_2 characterize the anisotropy of the path lengths used as an input to DREENA-B, which we had chosen to agree with the conventional models.² It is, however, much less trivial that through this procedure, in which we calculate the ratio of v_2 and $1 - R_{AA}$ through full DREENA framework, our *extracted* ϵ_{2L} almost exactly recovers our initial ϵ_2 . Note that ϵ_2 is *indirectly* introduced in R_{AA} and v_2 calculations through path-length distributions, while our calculations are performed using full-fledged numerical procedure, not just Eq. (1). Consequently, such direct extraction of ϵ_{2L} and its agreement with our initial (and consequently also conventional) ϵ_2 is highly nontrivial and gives us a good deal of confidence that $v_2/(1 - R_{AA})$ is related to the anisotropy of the system only, and not its material properties.

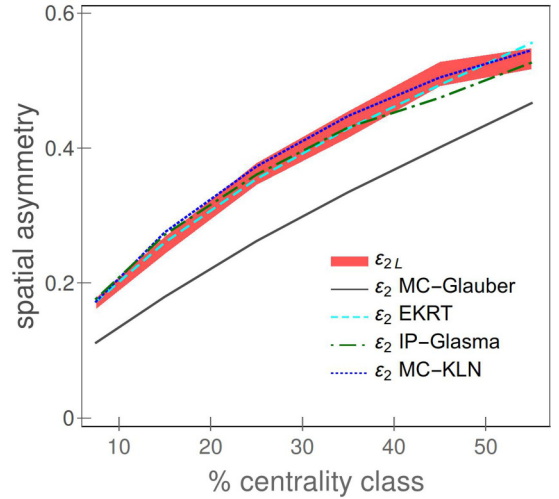


FIG. 3. Comparison of ϵ_{2L} (red band) obtained from our method, with ϵ_2 calculated using Monte Carlo (MC)-Glauber [39] (gray band), EKRT [40] (purple band), IP-Glasma [41] (green dot-dashed curve), and MC-KLN [42] (blue dotted curve) approaches. MC-Glauber and EKRT results correspond to 5.02 TeV, while IP-Glasma and MC-KLN correspond to 2.76 TeV Pb+Pb collisions at the LHC.

Summary. High- p_\perp theory and data are traditionally used to explore interactions of traversing high- p_\perp probes with QGP, while bulk properties of QGP are obtained through low- p_\perp data and the corresponding models. On the other hand, it is clear that high- p_\perp probes are also powerful tomography tools since they are sensitive to global QGP properties. We here demonstrated this in the case of spatial anisotropy of the QCD matter formed in ultrarelativistic heavy-ion collisions. We used our dynamical energy-loss formalism to show that a (modified) ratio of two main high- p_\perp observables, R_{AA} and v_2 , approaches an asymptotic limit at experimentally accessible transverse momenta, and that this asymptotic value depends only on the shape of the system, not on its material properties. However, how exactly this asymptotic value reflects the shape and anisotropy of the system requires further study employing full three-dimensional expansion, which is our current work in progress. The experimental accuracy does not yet allow the extraction of the anisotropy from the data using our scheme, but once the accuracy improves in the upcoming LHC runs, we expect that the anisotropy of the QGP formed in heavy-ion collisions can be inferred directly from the data. Such an experimentally obtained anisotropy parameter would provide an important constraint to models describing the early stages of heavy-ion collision and QGP evolution, and demonstrate synergy of high- p_\perp theory and data with more common approaches for inferring QGP properties.

Acknowledgments. We thank Jussi Auvinen, Hendrik van Hees, Etele Molnar, and Dusan Zigic for useful discussions. We also thank Tetsufumi Hirano and Harri Niemi for sharing their MC-KLN and EKRT results with us. This work is supported by the European Research Council, Grant No. ERC-2016-COG: 725741, and by the Ministry of Science and Technological Development of the Republic of Serbia, under Projects No. ON171004 and No. ON173052.

²Binary collision scaling calculated using optical Glauber model with additional cutoff in the tails of Woods-Saxon potentials, to be exact.

- [1] M. Gyulassy and L. McLerran, *Nucl. Phys. A* **750**, 30 (2005).
- [2] E. V. Shuryak, *Nucl. Phys. A* **750**, 64 (2005).
- [3] B. Jacak and P. Steinberg, *Phys. Today* **63**(5), 39 (2010).
- [4] C. V. Johnson and P. Steinberg, *Phys. Today* **63**(5), 29 (2010).
- [5] J. C. Collins and M. J. Perry, *Phys. Rev. Lett.* **34**, 1353 (1975).
- [6] G. Baym and S. A. Chin, *Phys. Lett. B* **62**, 241 (1976).
- [7] D. Zigic, I. Salom, J. Auvinen, M. Djordjevic, and M. Djordjevic, *J. Phys. G: Nucl. Part. Phys.* **46**, 085101 (2019).
- [8] T. Renk, *Phys. Rev. C* **85**, 044903 (2012).
- [9] D. Molnar and D. Sun, *Nucl. Phys. A* **932**, 140 (2014); **910-911**, 486 (2013).
- [10] D. Zigic, I. Salom, J. Auvinen, M. Djordjevic, and M. Djordjevic, *Phys. Lett. B* **791**, 236 (2019).
- [11] M. Djordjevic, D. Zigic, M. Djordjevic, and J. Auvinen, *Phys. Rev. C* **99**, 061902(R) (2019).
- [12] R. Baier, Y. Dokshitzer, A. Mueller, S. Peigne, and D. Schiff, *Nucl. Phys. B* **484**, 265 (1997).
- [13] N. Armesto, C. A. Salgado, and U. A. Wiedemann, *Phys. Rev. D* **69**, 114003 (2004).
- [14] M. Gyulassy, P. Lévai, and I. Vitev, *Nucl. Phys. B* **594**, 371 (2001).
- [15] X. N. Wang and X. f. Guo, *Nucl. Phys. A* **696**, 788 (2001).
- [16] M. Djordjevic and M. Djordjevic, *Phys. Rev. C* **92**, 024918 (2015).
- [17] A. Dainese (ALICE Collaboration), *Eur. Phys. J. C* **33**, 495 (2004).
- [18] S. Afanasiev *et al.* (PHENIX Collaboration), *Phys. Rev. C* **80**, 054907 (2009).
- [19] P. Christiansen, K. Tywoniuk, and V. Vislavicius, *Phys. Rev. C* **89**, 034912 (2014).
- [20] M. Djordjevic, *Phys. Rev. C* **80**, 064909 (2009); M. Djordjevic and U. Heinz, *Phys. Rev. Lett.* **101**, 022302 (2008).
- [21] M. Djordjevic, *Phys. Rev. C* **74**, 064907 (2006).
- [22] J. I. Kapusta, *Finite-Temperature Field Theory* (Cambridge University, New York, 1989).
- [23] M. Djordjevic and M. Gyulassy, *Phys. Rev. C* **68**, 034914 (2003).
- [24] M. Djordjevic and M. Djordjevic, *Phys. Lett. B* **709**, 229 (2012).
- [25] M. Djordjevic and M. Djordjevic, *Phys. Lett. B* **734**, 286 (2014).
- [26] B. Blagojevic, M. Djordjevic, and M. Djordjevic, *Phys. Rev. C* **99**, 024901 (2019).
- [27] Z. B. Kang, I. Vitev, and H. Xing, *Phys. Lett. B* **718**, 482 (2012).
- [28] M. Gyulassy, P. Levai, and I. Vitev, *Phys. Lett. B* **538**, 282 (2002).
- [29] D. de Florian, R. Sassot, and M. Stratmann, *Phys. Rev. D* **75**, 114010 (2007).
- [30] B. Blagojevic and M. Djordjevic, *J. Phys. G: Nucl. Part. Phys.* **42**, 075105 (2015).
- [31] Y. Maezawa, S. Aoki, S. Ejiri, T. Hatsuda, N. Ishii, K. Kanaya, N. Ukita, T. Umeda (WHOT-QCD Collaboration), *Phys. Rev. D* **81**, 091501(R) (2010).
- [32] A. Nakamura, T. Saito, and S. Sakai, *Phys. Rev. D* **69**, 014506 (2004).
- [33] S. Acharya *et al.* (ALICE Collaboration), *J. High Energy Phys.* **11** (2018) 013.
- [34] S. Acharya *et al.* (ALICE Collaboration), *J. High Energy Phys.* **07** (2018) 103.
- [35] V. Khachatryan *et al.* (CMS Collaboration), *J. High Energy Phys.* **04** (2017) 039.
- [36] A. M. Sirunyan *et al.* (CMS Collaboration), *Phys. Lett. B* **776**, 195 (2018).
- [37] ATLAS Collaboration, ATLAS-CONF-2017-012 (unpublished), <https://cds.cern.ch/record/2244824>.
- [38] M. Aaboud *et al.* (ATLAS Collaboration), *Eur. Phys. J. C* **78**, 997 (2018).
- [39] C. Loizides, J. Kamin, and D. d'Enterria, *Phys. Rev. C* **97**, 054910 (2018).
- [40] K. J. Eskola, H. Niemi, R. Paatelainen, and K. Tuominen, *Phys. Rev. C* **97**, 034911 (2018).
- [41] J. E. Bernhard, J. S. Moreland, S. A. Bass, J. Liu, and U. Heinz, *Phys. Rev. C* **94**, 024907 (2016).
- [42] T. Hirano, P. Huovinen, K. Murase, and Y. Nara, *Prog. Part. Nucl. Phys.* **70**, 108 (2013).



XXVIIIth International Conference on Ultrarelativistic Nucleus-Nucleus Collisions
(Quark Matter 2019)

From high p_{\perp} theory and data to inferring anisotropy of Quark-Gluon Plasma

Magdalena Djordjevic^a, Stefan Stojku^a, Dusan Zigic^a, Bojana Ilic^a, Jussi
Auvinen^a, Igor Salom^a, Marko Djordjevic^b and Pasi Huovinen^a

^a Institute of Physics Belgrade, University of Belgrade, Serbia

^b Faculty of Biology, University of Belgrade, Serbia

Abstract

High p_{\perp} theory and data are commonly used to study high p_{\perp} parton interactions with QGP, while low p_{\perp} data and corresponding models are employed to infer QGP bulk properties. On the other hand, with a proper description of high p_{\perp} parton-medium interactions, high p_{\perp} probes become also powerful tomography tools, since they are sensitive to global QGP features, such as different temperature profiles or initial conditions. This tomographic role of high p_{\perp} probes can be utilized to assess the spatial anisotropy of the QCD matter. With our dynamical energy loss formalism, we show that a (modified) ratio of R_{AA} and v_2 presents a reliable and robust observable for straightforward extraction of initial state anisotropy. We analytically estimated the proportionality between the $v_2/(1-R_{AA})$ and anisotropy coefficient ϵ_{2L} , and found surprisingly good agreement with full-fledged numerical calculations. Within the current error bars, the extraction of the anisotropy from the existing LHC data using this approach is still inaccessible. However, with the expected accuracy improvement in the upcoming LHC runs, the anisotropy of the QGP formed in heavy ion collisions can be straightforwardly derived from the data. Such a data-based anisotropy parameter would present an important test to models describing the initial stages of heavy-ion collision and formation of QGP, and demonstrate the usefulness of high p_{\perp} theory and data in obtaining QGP properties.

Keywords: Quark-gluon plasma, High p_{\perp} probes, Initial anisotropy

1. Introduction

Understanding the properties of the new form of matter named Quark-Gluon Plasma (QGP) is the major goal of relativistic heavy ion physics [1, 2]. However, to explore the properties of QGP, one needs good probes. With regards to that, it is commonly assumed that high p_{\perp} theory and data are good probes for exploring the high p_{\perp} parton interactions with QGP, while low p_{\perp} theory and data are considered as good probes for bulk QGP properties. Contrary to this common assumption, the goal of this contribution is to demonstrate that high p_{\perp} particles can also be useful independent probes of *bulk* QGP properties.

To put it simply, the main idea is that when high p_{\perp} particles transverse QGP, they lose energy, where this energy loss is sensitive to bulk QGP properties, such as its temperature profiles or initial conditions.

Consequently, with a realistic and sophisticated high p_{\perp} parton energy loss model, high p_{\perp} probes can indeed become powerful tomographic tools. So, in this contribution, we will present how we can use these probes to infer some of the bulk QGP properties, i.e., for precision QGP tomography. Note that only the main results are presented here; for a more detailed version, see [3], and references therein.

2. DREENA framework

To achieve the goal of utilizing high p_{\perp} theory and data for inferring the bulk QGP properties, as previously implied, a reliable high p_{\perp} parton energy loss model is necessary. With this goal in mind, we developed a dynamical energy loss formalism [4, 5], which takes into account some more realistic and unique features, such as: i) The calculations are performed within finite temperature field theory and generalized Hard-Thermal-Loop [6] approach, in which the infrared divergences are naturally regulated, excluding the need for artificial cutoffs. ii) The formalism assumes QCD medium of finite size and finite temperature, consisting of dynamical partons (i.e., energy exchange with medium constituents is included), in distinction to commonly considered static scatterers approximation and/or models with vacuum-like propagators. iii) Both radiative [4] and collisional [5] energy losses are calculated within the same theoretical framework, and are equally applicable to light and heavy flavors. iv) The formalism is generalized to include a finite chromomagnetic mass [7], running coupling, and to relax the widely used soft-gluon approximation [8]. Finally, the formalism is integrated in a numerical framework DREENA (Dynamical Radiative and Elastic ENergy loss Approach) [9, 10], to provide predictions for high p_{\perp} observables.

Within this framework, we generated a wide set of high p_{\perp} predictions using 1D Bjorken expansion [11] (i.e., DREENA-B framework [10]). Thus we obtained a good joint agreement with a wide range of high p_{\perp} R_{AA} and v_2 data, by applying the same numerical procedure, the same parameter set, and no fitting parameters in model testing. That is, there is no v_2 puzzle [12] within our model, which then strongly suggests that the model provides a realistic description of high p_{\perp} parton-medium interactions. Moreover, our preliminary findings suggest that, within our formalism, moving from 1D Bjorken to full 3D hydrodynamical expansion does not significantly affect the agreement of our predictions with high p_{\perp} R_{AA} and v_2 data [13]. Consequently, in order to adequately address the high p_{\perp} measurements, a proper description of high p_{\perp} parton interactions with the medium appears to be much more important than an advanced medium evolution description. Furthermore, we have also analyzed the sensitivity of high p_{\perp} R_{AA} and v_2 to different initial stages, giving an additional insight in the usefulness of both high p_{\perp} observables in the precision QGP tomography [14].

3. Inferring QGP anisotropy through high p_{\perp} theory and data

As one example of QGP tomography, in this contribution, we will address how to infer the QGP anisotropy from high p_{\perp} R_{AA} and v_2 data. The initial state anisotropy is one of the main properties of QGP and a major limiting factor for precision QGP tomography. However, despite its essential importance, it is still not possible to directly infer the initial anisotropy from experimental measurements. Several theoretical studies [15, 16, 17, 18] have provided different methods for calculating the initial anisotropy, leading to notably different predictions, with a notable effect in the resulting predictions for both low and high p_{\perp} data. Therefore, approaches for inferring anisotropy from the data are necessary. Optimally, these approaches should be complementary to existing predictions, i.e., based on a method that is fundamentally different from models of early stages of QCD matter.

To this end, we here propose a novel approach to extract the initial state anisotropy. Our method is based on inference from high p_{\perp} data, by using already available R_{AA} and v_2 measurements, which will moreover be measured with much higher precision in the future. Such an approach is substantially different from the existing approaches, as it is based on the inference from experimental data (rather than on calculations of early stages of QCD matter) exploiting the information from interactions of rare high p_{\perp} partons with the QCD medium. This also presents an improvement/optimization in utilizing high p_{\perp} data as, to date, these data were mostly constrained on studying the parton-medium interactions, rather than assessing bulk QGP parameters, such as spatial asymmetry.

In the literature, the initial state anisotropy is quantified in terms of eccentricity parameter ϵ_2

$$\epsilon_2 = \frac{\langle y^2 - x^2 \rangle}{\langle y^2 + x^2 \rangle} = \frac{\int dx dy (y^2 - x^2) \rho(x, y)}{\int dx dy (y^2 + x^2) \rho(x, y)}, \quad (1)$$

where $\rho(x, y)$ denotes the initial density distribution of the formed QGP. Regarding high p_\perp observables, we note that v_2 is sensitive to both the anisotropy of the system and its size, while R_{AA} is sensitive only to the size of the system. Therefore, it is plausible that the adequate observable for extracting eccentricity from high p_\perp data depends on both v_2 and R_{AA} , and the question is how.

To address this question, we will use the dynamical energy loss formalism, and DREENA-B framework outlined above. For high p_\perp , the fractional energy loss scales as [3] $\Delta E/E \sim \chi \langle T \rangle^a \langle L \rangle^b$, where $\langle T \rangle$ stands for the average temperature along the path of high p_\perp parton, $\langle L \rangle$ is the average path-length traversed by the parton, χ is a proportionality factor that depends on the initial parton transverse momentum, and a and b are exponents which govern the temperature and path-length dependence of the energy loss. Within our model, $a \approx 1.2$ and $b \approx 1.4$, which is contrary to simpler models, and consistent with a wide range of experimental data [19, 20]. From this simple scaling argument, we can straightforwardly obtain the following expressions for R_{AA} and v_2 (for more details we refer the reader to [3]):

$$R_{AA} \approx 1 - \xi(\chi) \langle T \rangle^a \langle L \rangle^b, \quad v_2 \approx \frac{1}{2} \frac{R_{AA}^{in} - R_{AA}^{out}}{R_{AA}^{in} + R_{AA}^{out}} \approx \xi(\chi) \langle T \rangle^a \langle L \rangle^b \left(\frac{b}{2} \frac{\Delta L}{\langle L \rangle} - \frac{a}{2} \frac{\Delta T}{\langle T \rangle} \right), \quad (2)$$

where we see that $\xi(\chi) \langle T \rangle^a \langle L \rangle^b$ corresponds to $1 - R_{AA}$. Therefore, if we divide v_2 by $(1 - R_{AA})$, we see that this ratio is given by the following simple expression:

$$\frac{v_2}{1 - R_{AA}} \approx \left(\frac{b}{2} \frac{\Delta L}{\langle L \rangle} - \frac{a}{2} \frac{\Delta T}{\langle T \rangle} \right). \quad (3)$$

Note that, while this ratio exposes the dependence on the asymmetry of the system (through spatial $(\Delta L/\langle L \rangle)$ and temperature $(\Delta T/\langle T \rangle)$ parts), the dependence only on spatial anisotropy is still not isolated. However, by plotting together spatial and temperature anisotropy, we obtain a linear dependence [3], with a proportionality factor given by $c \approx 4.3$. Therefore, $v_2/(1 - R_{AA})$ reduces to the following expression:

$$\frac{v_2}{1 - R_{AA}} \approx \frac{1}{2} \left(b - \frac{a}{c} \right) \frac{\langle L_{out} \rangle - \langle L_{in} \rangle}{\langle L_{out} \rangle + \langle L_{in} \rangle} \approx 0.57\zeta, \quad \text{where } \zeta = \frac{\langle L_{out} \rangle - \langle L_{in} \rangle}{\langle L_{out} \rangle + \langle L_{in} \rangle} \text{ and } \frac{1}{2} \left(b - \frac{a}{c} \right) \approx 0.57. \quad (4)$$

Consequently, the asymptotic scaling behavior of observables v_2 and R_{AA} , at high p_\perp , reveals that their (moderated) ratio is determined only by the geometry of the initial QGP droplet. Therefore, the anisotropy parameter ζ could, in principle, be directly obtained from the high p_\perp experimental data.

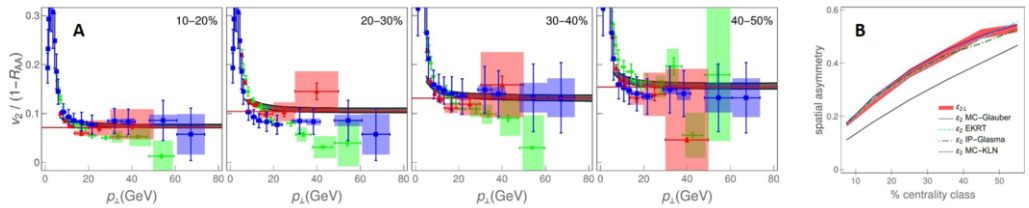


Fig. 1. **A)** Comparison of theoretical predictions for charged hadron $v_2/(1 - R_{AA})$ as a function of p_\perp with 5.02 TeV $Pb + Pb$ CMS [21, 22] (blue squares), ALICE [23, 24] (red triangles) and ATLAS [25, 26] (green circles) data. Each panel corresponds to different centrality range, as indicated in the upper right corners, while red lines denote the limit 0.57ζ from Eq. (4). **B)** Comparison of ϵ_{2L} (red band) extracted from our full-fledged calculations, with ϵ_2 obtained from MC-Glauber [15] (gray full curve), EKRT [16] (cyan dashed curve), IP-Glasma [17] (green dot-dashed curve) and MC-KLN [18] (blue dotted curve) models. MC-Glauber and EKRT curves correspond to 5.02 TeV, whereas IP-Glasma and MC-KLN curves correspond to 2.76 TeV $Pb + Pb$ collisions at the LHC.

To test the adequacy of the analytical estimate given by Eqs. (2)-(4), Fig. 1A is displayed, which comprises our $v_2/(1 - R_{AA})$ predictions (gray bands), stemming from our full-fledged recently developed

DREENA-B framework (outlined in the previous section), the ALICE, CMS and ATLAS data, and analytically derived asymptote 0.57ζ (red lines). Importantly, for each centrality range and for $p_{\perp} \gtrsim 20$ GeV, $v_2/(1 - R_{AA})$ is independent on p_{\perp} , and approaches the asymptote, i.e., is determined by the geometry of the system - depicted by the solid red line, up to 5% accuracy. Moreover, the experimental data for all three experiments also display the independence on the p_{\perp} and agree with our predictions, although the error bars are rather large. Therefore, we conclude that our scaling estimates are valid and that $v_2/(1 - R_{AA})$ indeed carries the information about the anisotropy of the fireball, which can be simply (from the straight line fit to data at high p_{\perp} limit) and robustly (in the same way for each centrality) inferred from the experimental data.

However, note that the anisotropy parameter ζ is not the widely-considered anisotropy parameter ϵ_2 (given by Eq. (1)). To facilitate comparison with ϵ_2 values in the literature, we define $\epsilon_{2L} = \frac{(L_{out})^2 - (L_{in})^2}{(L_{out})^2 + (L_{in})^2} = \frac{2\zeta}{1+\zeta^2}$, and in Fig. 1B compare it with the results from different initial-state models [15, 16, 17, 18]. First, we should note that as a starting point, our initial ϵ_2 , through which we generate our path-length distributions, agrees with EKRT and IP-Glasma. However, what is highly non-trivial is that, as an outcome of this procedure, in which $v_2/(1 - R_{AA})$ is calculated (based on the full-fledged DREENA-B framework), we obtain ϵ_{2L} which practically coincides with our initial ϵ_2 and also with some of the conventional initial-state models. As an overall conclusion, the straightforward extraction of ϵ_{2L} and its agreement with values of the prevailing initial-state models' eccentricity (and our initial ϵ_2) is highly non-trivial and supports $v_2/(1 - R_{AA})$ as a reliable and robust observable for anisotropy. Additionally, the width of our ϵ_{2L} band is smaller than the difference in the ϵ_2 values obtained by using different models (e.g., MC-Glauber vs. MC-KLN). Therefore, our approach provides genuine resolving power to distinguish between different initial-state models, although it may not be possible to separate the finer details of more sophisticated models. This resolving power, moreover, comes from an entirely different perspective, i.e., from high p_{\perp} theory and data, supporting the usefulness of utilizing high p_{\perp} theory and data for inferring the bulk QGP properties.

Acknowledgements: This work is supported by the European Research Council, grant ERC-2016-COG: 725741, and by the Ministry of Science and Technological Development of the Republic of Serbia, under project numbers ON171004, ON173052 and ON171031.

References

- [1] M. Gyulassy and L. McLerran, Nucl. Phys. A **750**, 30 (2005); E. V. Shuryak, Nucl. Phys. A **750**, 64 (2005).
- [2] B. Jacak and P. Steinberg, Phys. Today **63**, 39 (2010); C. V. Johnson and P. Steinberg, Phys. Today **63**, 29 (2010).
- [3] M. Djordjevic, S. Stojku, M. Djordjevic and P. Huovinen, Phys. Rev. C **100**, no. 3, 031901 (2019).
- [4] M. Djordjevic, Phys. Rev. C **80**, 064909 (2009); M. Djordjevic and U. Heinz, Phys. Rev. Lett. **101**, 022302 (2008).
- [5] M. Djordjevic, Phys. Rev. C **74**, 064907 (2006).
- [6] J. I. Kapusta, *Finite-Temperature Field Theory* (Cambridge University Press, 1989).
- [7] M. Djordjevic and M. Djordjevic, Phys. Lett. B **709**, 229 (2012).
- [8] B. Blagojevic, M. Djordjevic and M. Djordjevic, Phys. Rev. C **99**, 024901 (2019).
- [9] D. Zigic, I. Salom, J. Auvinen, M. Djordjevic and M. Djordjevic, J. Phys. G **46**, 085101 (2019).
- [10] D. Zigic, I. Salom, M. Djordjevic and M. Djordjevic, Phys. Lett. B **791**, 236 (2019).
- [11] J. D. Bjorken, Phys. Rev. D **27**, 140 (1983).
- [12] J. Noronha-Hostler, B. Betz, J. Noronha and M. Gyulassy, Phys. Rev. Lett. **116**, no. 25, 252301 (2016); B. Betz and M. Gyulassy, JHEP **1408**, 090 (2014); S. K. Das, F. Scardina, S. Plumari and V. Greco, Phys. Lett. B **747**, 260 (2015).
- [13] D. Zigic, *et al.*, to be submitted.
- [14] D. Zigic, B. Ilic, M. Djordjevic and M. Djordjevic, arXiv:1908.11866 [hep-ph].
- [15] C. Loizides, J. Kamin and D. d'Enterria, Phys. Rev. C **97**, 054910 (2018).
- [16] K. J. Eskola, H. Niemi, R. Paatelainen and K. Tuominen, Phys. Rev. C **97**, 034911 (2018).
- [17] J. E. Bernhard, J. S. Moreland, S. A. Bass, J. Liu and U. Heinz, Phys. Rev. C **94**, 024907 (2016).
- [18] T. Hirano, P. Huovinen, K. Murase and Y. Nara, Prog. Part. Nucl. Phys. **70**, 108 (2013).
- [19] M. Djordjevic and M. Djordjevic, Phys. Rev. C **92**, 024918 (2015).
- [20] M. Djordjevic, D. Zigic, M. Djordjevic and J. Auvinen, Phys. Rev. C **99**(R), 061902 (2019).
- [21] V. Khachatryan *et al.* [CMS Collaboration], JHEP **1704**, 039 (2017).
- [22] A. M. Sirunyan *et al.* [CMS Collaboration], Phys. Lett. B **776**, 195 (2018).
- [23] S. Acharya *et al.* [ALICE Collaboration], JHEP **1811**, 013 (2018).
- [24] S. Acharya *et al.* [ALICE Collaboration], JHEP **1807**, 103 (2018).
- [25] [ATLAS Collaboration], ATLAS-CONF-2017-012.
- [26] M. Aaboud *et al.* [ATLAS Collaboration], Eur. Phys. J. C **78**, no. 12, 997 (2018).

Extracting the temperature dependence in high- p_{\perp} particle energy lossStefan Stojku ¹, Bojana Ilic ¹, Marko Djordjevic ² and Magdalena Djordjevic ^{1,*}¹*Institute of Physics Belgrade, University of Belgrade, Belgrade, Serbia*²*Faculty of Biology, University of Belgrade, Belgrade, Serbia*

(Received 16 July 2020; accepted 2 February 2021; published 16 February 2021)

The suppression of high- p_{\perp} particles is one of the main signatures of parton energy loss during its passing through the quark-gluon plasma medium, and is reasonably reproduced by different theoretical models. However, a decisive test of the reliability of a certain energy-loss mechanism, apart from its path length, is its temperature dependence. Despite its importance and comprehensive dedicated studies, this issue is still awaiting more stringent constraints. To this end, we here propose a novel observable to extract the temperature-dependence exponent of a high- p_{\perp} particle's energy loss, based on R_{AA} . More importantly, by combining analytical arguments, full-fledged numerical calculations, and comparison with experimental data, we argue that this observable is highly suited for testing the long-standing $\Delta E/E \propto L^2 T^3$ paradigm. The anticipated significant reduction of experimental errors will allow direct extraction of temperature dependence, by considering different centrality pairs in $A + A$ collisions (irrespective of the nucleus size) in the high- p_{\perp} region. Overall, our results imply that this observable, which reflects the underlying energy-loss mechanism, is very important to distinguish between different theoretical models.

DOI: [10.1103/PhysRevC.103.024908](https://doi.org/10.1103/PhysRevC.103.024908)**I. INTRODUCTION**

The main goal of the ultrarelativistic heavy-ion program [1–4] at the Relativistic Heavy Ion Collider (RHIC) and the Large Hadron Collider (LHC) is inferring the features of the created novel form of matter—quark-gluon plasma (QGP) [5,6]—which provides an insight into the nature of the hottest and densest known medium. Energy loss of rare high- p_{\perp} partons traversing the medium is considered to be one of the crucial probes [7] of the medium properties, which also had a decisive role in QGP discovery [8]. Comparison of predictions stemming from different energy-loss models with experimental data tests our understanding of the mechanisms underlying the jet-medium interactions, thereby illuminating the QGP properties. Within this, an important goal involves a search for adequate observables for distinguishing the energy-loss mechanisms.

Connected to this, it is known that the temperature (T) dependence of the energy-loss predictions may be related to the underlying energy-loss mechanisms; e.g., pQCD *radiative* energy loss (Baier-Dokshitzer-Mueller-Peigne-Schiff (BDMPS) and Armesto-Salgado-Wiedemann (ASW) [9–11], Gyulassy-Levai-Vitev (GLV) [12], light-cone path integral (LCPI) [13] and Arnold-Moore-Yaffe (AMY) [14], higher-twist (HT) [15], and some of their extensions [16–20]) is typically considered to have cubic T dependence (T^3 , stemming from entropy, or energy density dependence), while *collisional* energy loss [7,21–23] is generally considered to be proportional to T^2 . Additionally, anti-de Sitter/conformal field

theory (AdS/CFT)-motivated jet-energy-loss models [24,25] display even quartic (T^4) dependence on temperature. The different functional dependences on T found in these models are the results of the considered energy-loss mechanism (elastic or inelastic), different treatment of the QCD medium (finite or infinite size), and inclusion or omission of finite temperature effects (i.e., application of temperature-modified or vacuumlike propagators). Therefore, assessing the accurate temperature dependence is important for disentangling relevant effects for adequate description of leading parton energy loss, and consequently for understanding the QGP properties.

For a comprehensive study on temperature (and path-length) dependence of different energy-loss models we refer the reader to Ref. [18]. However, even this systematic study could not single out local T dependence, as the attempt to simultaneously describe high- p_{\perp} R_{AA} and v_2 data within these models requires some more rigorous physical justifications. Moreover, the current error bars at the RHIC and the LHC are still too large to resolve between different energy-loss models. Having this in mind, we here propose a novel observable to extract the scaling of a high- p_{\perp} particle's energy loss on the local temperature. Note that, for extracting the exact value of the temperature-dependence exponent, this new observable relies on the previously extracted value of the path-length dependence coefficient [26]. We expect that this observable will allow direct extraction of T dependence from the data in the upcoming high-luminosity third run at the LHC, where the error bars are expected to notably decrease.

We also propose high- p_{\perp} h^{\pm} as the most suitable probe for this paper, as the experimental data for h^{\pm} R_{AA} are more abundant and with smaller error bars, compared to heavier hadrons for all centrality classes, where this is also expected

*magda@ipb.ac.rs

to hold in the future. Therefore, in this paper, we concentrate on h^\pm in 5.02-TeV Pb + Pb collisions at the LHC, with the goal to elucidate this new observable, and test its robustness to medium evolution and colliding system size. By combining full-fledged numerical predictions and scaling arguments within our dynamical radiative and elastic energy-loss approach (DREENA) [27,28] framework, this new observable yields the value of the temperature-dependence exponent, which is in accordance with our previous estimate [29]. More importantly, we utilize this observable to question the long-standing $\Delta E/E \propto L^2 T^3$ paradigm, used in a wide range of theoretical models [9–12,15–20].

II. THEORETICAL FRAMEWORK

In this paper, we use our state-of-the-art dynamical energy-loss formalism [30–32], which includes several unique features in modeling jet-medium interactions: (1) calculations within the finite temperature field theory and generalized hard-thermal-loop approach [33] (contrary to many models

which apply vacuumlike propagators [9,10,12,15]), so that infrared divergences are naturally regulated in a highly non-trivial manner; (2) finite size of created QGP; (3) the QCD medium consisting of dynamical (moving) as opposed to static scattering centers, which allows the longitudinal momentum exchange with the medium constituents; (4) both radiative [30,31] and collisional [32] contributions calculated within the same theoretical framework; (5) the inclusion of a finite parton's mass [34], making the formalism applicable to both light and heavy flavor; and (6) the generalization to a finite magnetic mass [35], running coupling [36], and beyond soft-gluon approximation [37]. Note, however, that in Ref. [37] we obtained that the effect of relaxing the soft-gluon approximation on (fractional radiative energy loss and) R_{AA} is negligible, and thus can be omitted without losing the reliability of the obtained results. Therefore, to avoid unnecessary involvement of already complex expressions we here apply their soft-gluon equivalents.

The analytical expression for the single gluon radiation spectrum reads [27,30,35,36]

$$\frac{dN_{\text{rad}}}{dx d\tau} = \frac{C_2(G)C_R}{\pi} \frac{1}{x} \int \frac{d^2\mathbf{q}}{\pi} \frac{d^2\mathbf{k}}{\pi} \frac{\mu_E^2(T) - \mu_M^2(T)}{[\mathbf{q}^2 + \mu_E^2(T)][\mathbf{q}^2 + \mu_M^2(T)]} T \alpha_s(ET) \alpha_s \left(\frac{\mathbf{k}^2 + \chi(T)}{x} \right) \times \left[1 - \cos \left(\frac{(\mathbf{k} + \mathbf{q})^2 + \chi(T)}{xE^+} \tau \right) \right] \frac{2(\mathbf{k} + \mathbf{q})}{(\mathbf{k} + \mathbf{q})^2 + \chi(T)} \left[\frac{\mathbf{k} + \mathbf{q}}{(\mathbf{k} + \mathbf{q})^2 + \chi(T)} - \frac{\mathbf{k}}{\mathbf{k}^2 + \chi(T)} \right], \quad (1)$$

where \mathbf{k} and \mathbf{q} denote transverse momenta of radiated and exchanged gluons, respectively; $C_2(G) = 3$ and $C_R = 4/3$ ($C_R = 3$) for the quark (gluon) jet; while $\mu_E(T)$ and $\mu_M(T)$ are electric (Debye) and magnetic screening masses, respectively. The temperature-dependent Debye mass [27,38] is obtained by self-consistently solving Eq. (5) from Ref. [27]. α_s is the (temperature-dependent) running coupling [27,36,39], E is

the initial parton energy, while $\chi(T) = M^2 x^2 + m_g^2(T)$, where x is the longitudinal momentum fraction of the initial parton carried away by the emitted gluon. M is the mass of the propagating parton, while the gluon mass is considered to be equal to its asymptotical mass $m_g = \mu_E/\sqrt{2}$ [40].

The analytical expression for collisional energy loss per unit length is given by the following expression [27,32]:

$$\frac{dE_{\text{coll}}}{d\tau} = \frac{2C_R}{\pi v^2} \alpha_s(ET) \alpha_s(\mu_E^2(T)) \int_0^\infty n_{\text{eq}}(|\vec{\mathbf{k}}|, T) d|\vec{\mathbf{k}}| \times \left[\int_0^{|\vec{\mathbf{k}}|/(1+v)} d|\vec{\mathbf{q}}| \int_{-v|\vec{\mathbf{q}}|}^{v|\vec{\mathbf{q}}|} \omega d\omega + \int_{|\vec{\mathbf{k}}|/(1+v)}^{|\vec{\mathbf{q}}|_{\text{max}}} d|\vec{\mathbf{q}}| \int_{|\vec{\mathbf{q}}|-2|\vec{\mathbf{k}}|}^{v|\vec{\mathbf{q}}|} \omega d\omega \right] \times \left[|\Delta_L(q, T)|^2 \frac{(2|\vec{\mathbf{k}}| + \omega)^2 - |\vec{\mathbf{q}}|^2}{2} + |\Delta_T(q, T)|^2 \frac{(|\vec{\mathbf{q}}|^2 - \omega^2)[(2|\vec{\mathbf{k}}| + \omega)^2 + |\vec{\mathbf{q}}|^2]}{4|\vec{\mathbf{q}}|^4} (v^2|\vec{\mathbf{q}}|^2 - \omega^2) \right], \quad (2)$$

where $n_{\text{eq}}(|\vec{\mathbf{k}}|, T) = \frac{N}{e^{|\vec{\mathbf{k}}|/T-1}} + \frac{N_f}{e^{|\vec{\mathbf{k}}|/T+1}}$ is the equilibrium momentum distribution [22] including gluons, quarks, and antiquarks. k is the four-momentum of the incoming medium parton, v is the velocity of the initial jet, and $q = (\omega, \vec{\mathbf{q}})$ is the four-momentum of the exchanged gluon. $|\vec{\mathbf{q}}|_{\text{max}}$ is provided in Ref. [32], while $\Delta_T(q, T)$ and $\Delta_L(q, T)$ are effective transverse and longitudinal gluon propagators given by Eqs. (3) and (4) from Ref. [27].

Despite the very complicated temperature dependence of Eqs. (1) and (2), in Ref. [29] it was obtained that our dynamical energy-loss formalism [36] (which accommodates

some unique jet-medium effects mentioned above) has an exceptional feature of near linear T dependence. That is, while T^3 dependence for radiative energy loss is widely used [9–12,14–20], from Eq. (1) it is evident that this simplified relation is reproduced with approximations using vacuum gluon propagators (leading to the absence of $m_g(T)$ from the χ expression) and neglecting running coupling. It is straightforward to show that in that case leading T dependence is $\frac{\Delta E_{\text{rad}}}{E} \propto \mu_E^2 T \propto T^3$ ($\mu_E \propto T$). However, Eq. (1) clearly demonstrates that a more realistic T dependence is far from cubic, where in Ref. [29] it was shown that asymptotic T dependence

of our full radiative energy loss is between linear and quadratic.

Additionally, commonly overlooked (due to being smaller compared to radiative at high p_{\perp}) collisional energy loss must not be neglected in suppression predictions [41]. Moreover, widely used dominant T^2 dependence of collisional energy loss [7,21–23] can also be shown to be a consequence of (i) using tree-level diagrams, and consequently introducing artificial cutoffs to nonphysically regulate ultraviolet (and infrared) divergencies (e.g., in Ref. [7]) in the hard momentum transfer sector [22]; or (ii) considering only soft momentum exchange [21]. That is, it is straightforward to show that Eq. (2) recovers leading T^2 dependence from Ref. [21] if (1) only the soft gluon sector is considered, with the upper limit of integration artificially set to $|\vec{q}|_{\max}$; (2) only forward emission is accounted for ($\omega > 0$); and (3) running coupling is neglected. Accordingly, in Ref. [29] it was demonstrated that complex T dependence of our *collisional energy loss* (Eq. (2)) reduces not to commonly considered quadratic, but rather to nearly linear dependence for asymptotically large p_{\perp} . Therefore, a state-of-the-art energy-loss model leads to a much slower growth of the energy loss with temperature compared to the common paradigm, where the widely assumed faster growth can be reproduced only through quite drastic simplifying assumptions.

Since the goal of this paper is the extraction of the temperature-dependence exponent of the energy loss, this paper will furthermore provide an opportunity to test our dynamical energy-loss formalism on a more basic level.

III. NUMERICAL FRAMEWORK

In this paper, the predictions are generated within our fully optimized DREENA [27,28] numerical framework, comprising (i) initial parton momentum distribution [42]; (ii) energy-loss probability based on our dynamical energy-loss formalism [30–32] (discussed in the previous section), which includes multigluon [43] and path-length fluctuations [44], where the path-length fluctuations are calculated according to the procedure provided in Ref. [45] (see also Ref. [28]); and (iii) fragmentation functions [46]. In this paper, we will primarily use two implementations of this framework: (i) DREENA-C, where C corresponds to constant temperature medium; and (ii) DREENA-B, where B corresponds to one-dimensional (1D) Bjorken QGP evolution [7].

In the first part of our paper, using the DREENA-C framework, the average temperature is obtained according to the procedure described in Refs. [28,47], which we briefly outline here. For each centrality region in 5.02-TeV Pb + Pb collisions, the average temperature is estimated through $T^3 \sim \frac{dN_g}{dy} \frac{1}{A_{\perp} L}$ [12,48], where A_{\perp} is the overlap area. $\frac{dN_g}{dy}$ is gluon rapidity density, and is shown to be directly proportional to charged particle multiplicity $\frac{dN_{\text{ch}}}{d\eta}$, which is measured for all relevant centralities in 5.02-TeV Pb + Pb collisions at the LHC [49]. Thus, the required expression reads $T = c \left(\frac{dN_{\text{ch}}}{A_{\perp} L} \right)^{\frac{1}{3}}$, where constant c can be fixed by effective temperature for 0–20% 2.76-TeV Pb+Pb collisions at LHC [50], leading to, e.g., the average medium temperature of 348 MeV [47,50] in most central 5.02-TeV Pb + Pb collisions at the LHC.

In the second part of this paper, where we use the DREENA-B framework to test the sensitivity of the obtained results, the initial temperature (T_0) for each centrality is estimated in accordance with Ref. [27]. That is, for each centrality class, T_0 is determined in accordance with $T_0 \sim \left(\frac{dN_{\text{ch}}}{A_{\perp} L} \right)^{\frac{1}{3}}$ [51]. As a starting point, $T_0 = 500$ MeV in most central 5.02-TeV Pb + Pb collisions at the LHC is estimated from the average medium temperature of 348 MeV [47,50] in these collisions (see above), and a QCD transition temperature of $T_c \approx 155$ MeV [52]. By knowing T_0 in the most central 5.02-TeV Pb + Pb collision, based on the expression above, it is straightforward to obtain T_0 s for different centralities. In both studies, the average path lengths (L) for different centrality classes have been calculated by integrating the path-length distributions [28] which were obtained by following the procedure outlined in Ref. [45], with an additional hard-sphere restriction $r < R_A$ in the Woods-Saxon nuclear density distribution to regulate the path lengths in the peripheral collisions.

In generating numerical predictions, all the parameters correspond to standard literature values, i.e., we use no fitting parameters. We consider a QGP with $n_f = 3$ and $\Lambda_{\text{QCD}} = 0.2$ GeV. For the light quarks we assume that their mass is dominated by the thermal mass $M \approx \mu_E / \sqrt{6}$. The magnetic to electric mass ratio is assumed to be $0.4 < \mu_M / \mu_E < 0.6$ [53,54].

IV. RESULTS AND DISCUSSION

In this section, we first address the choice of the suitable observable for extracting energy-loss temperature dependence. For this purpose, an observable which is sensitive only to the details of jet-medium interactions (to facilitate extraction of T dependence), rather than the subtleties of medium evolution (to avoid unnecessary complications and ensure robustness), would be optimal. R_{AA} has such features, since it was previously reported that it is very sensitive to energy-loss effects [41] and the average medium properties, while being practically insensitive to the details of medium evolution (as opposed to v_2) [26–28,55,56]. Therefore, it is plausible that the appropriate observable should be closely related to R_{AA} .

Our theoretical and numerical approaches described above (where the dynamical energy loss explicitly depends on T) are implemented in a fully optimized DREENA framework [27,28], which makes it suitable for this paper. To more easily interpret the obtained results, we start from a constant T medium, i.e., DREENA-C [28]. In this framework, the local temperature becomes the average (constant) temperature—this makes the extraction of the temperature dependence straightforward, which is the main advantage of that framework. To confirm that, through such procedure, we indeed extracted the local temperature dependence, we will use DREENA-B [27] as a crosscheck, as this more complex model incorporates medium evolution through 1D Bjorken longitudinal expansion [7]. We here exploit that DREENA-C and DREENA-B are analytically tractable, allowing us to derive the appropriate scaling behavior. Finally, as a check of sensitivity of our proposed observable to the details of the medium evolution we employ our DREENA-A framework (“A” stands

for “adaptive”), which employs state-of-the-art full three- plus one-dimensional (3+1D) hydrodynamical evolution.

With the intention of extracting simple functional dependence on T (of the otherwise analytically and numerically quite complex dependence of the fractional energy loss; see Eqs. (1) and (2)), we first provide the scaling arguments within the DREENA-C [28] framework. These scaling (analytical) arguments will then be followed by a full-fledged numerical analysis. Namely, in Refs. [26–28,43] it was shown that, at very large values of transverse momentum p_{\perp} and/or in peripheral collisions, the following estimates can be made:

$$\begin{aligned}\Delta E/E &\approx \eta T^a L^b, \\ R_{AA} &\approx 1 - \xi T^a L^b,\end{aligned}\quad (3)$$

where η denotes a proportionality factor, depending on initial parton transverse momentum and its flavor, while $\xi = (n - 2)\eta/2$, where n is the steepness of a power-law fit to the initial transverse momentum distribution, i.e., $d\sigma/dp_{\perp}^2 \propto p_{\perp}^{-n}$. T and L denote the average temperature (of the QCD medium) along the jet path and the average path length traversed by the energetic parton. The scaling factors for temperature and path-length energy-loss dependence are denoted as a and b , respectively.

We next formulate the quantity R_{AA}^T , with the goal to isolate the temperature dependence:

$$R_{AA}^T = \frac{1 - R_{AA}}{1 - R_{AA}^{\text{ref}}}, \quad (4)$$

which presents the $(1 - R_{AA})$ ratio for a pair of two different centrality classes. The centrality class that corresponds to R_{AA}^{ref} (i.e., the quantity in the denominator) is denoted as the referent centrality, and is always lower (corresponding to a more central collision) than centrality in the numerator. We term this new quantity, given by Eq. (4), as a *temperature-dependent suppression ratio* (R_{AA}^T), which we will further elucidate below.

Namely, by using Eq. (3), it is straightforward to isolate average T and average path-length dependence of R_{AA}^T :

$$R_{AA}^T = \frac{1 - R_{AA}}{1 - R_{AA}^{\text{ref}}} \approx \frac{\xi T^a L^b}{\xi T_{\text{ref}}^a L_{\text{ref}}^b} = \left(\frac{T}{T_{\text{ref}}}\right)^a \left(\frac{L}{L_{\text{ref}}}\right)^b, \quad (5)$$

which in logarithmic form reads

$$\ln(R_{AA}^T) = \ln\left(\frac{1 - R_{AA}}{1 - R_{AA}^{\text{ref}}}\right) \approx a \ln\left(\frac{T}{T_{\text{ref}}}\right) + b \ln\left(\frac{L}{L_{\text{ref}}}\right). \quad (6)$$

However, the remaining dependence of the newly defined quantity on the path length is undesired for the purpose of this paper. So, in order to make use of the previous equation, we first test how the two terms on the right-hand side of Eq. (6) are related. To this end, in Fig. 1 we plot $\ln(L/L_{\text{ref}})$ against $\ln(T/T_{\text{ref}})$ for several combinations of centralities, as denoted in the caption of Fig. 1.

Conveniently, Fig. 1 shows a linear dependence $\ln(L/L_{\text{ref}}) \approx k \ln(T/T_{\text{ref}})$, with $k \approx 1.86$. This leads to a simple relation:

$$\ln(R_{AA}^T) \approx (a + kb) \ln\left(\frac{T}{T_{\text{ref}}}\right), \quad (7)$$

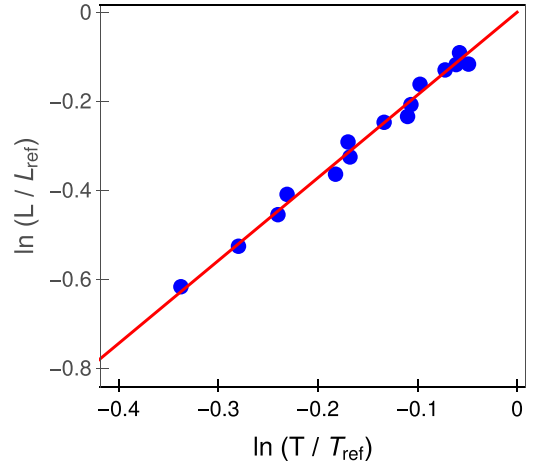


FIG. 1. $\ln(L/L_{\text{ref}})$ vs $\ln(T/T_{\text{ref}})$ in 5.02-TeV Pb+Pb collisions at the LHC for various centrality pairs. The referent centralities (for quantities in denominators) acquire one of the values 5–10, 10–20, 20–30, 30–40, or 40–50%, while the centralities in the numerator are always higher (the highest one being 50–60%). The solid red line corresponds to the linear fit to the calculated points.

so that with $f = a + kb$

$$R_{AA}^T \approx \left(\frac{T}{T_{\text{ref}}}\right)^f, \quad (8)$$

where this simple form facilitates extraction of a .

In Eq. (8), R_{AA}^T depends solely on T and effectively the temperature-dependence exponent a (as k and b [26] are known), which justifies the use of the “temperature-sensitive” term with this new quantity. Therefore, here we propose R_{AA}^T , given by Eq. (4), as a new observable, which is highly suitable for the purpose of this paper. Note, however, that this coupled dependence of R_{AA}^T on a and b exponents has its advantage, since it allows using this new observable to shed light on the underlying energy-loss mechanisms, by differentiating between various energy-loss models on both their T and L dependences.

The proposed extraction method is the following: We use our full-fledged DREENA-C numerical procedure to generate predictions for R_{AA} and thereby for the left-hand side of Eq. (8). Calculation of average T is already outlined in the previous section and described in detail above. We will generate the predictions with a full-fledged procedure, where we expect asymptotic scaling behavior (given by Eq. (8)) to be valid at high $p_{\perp} \approx 100$ GeV. Having in mind that values of k and b parameters have been extracted earlier, the temperature-dependence exponent a in the very high- p_{\perp} limit can then be estimated from the slope (f) of a $\ln(R_{AA}^T)$ vs $\ln(T/T_{\text{ref}})$ linear fit, done for a variety of centrality pairs.

However, before embarking on this task, we first verify whether our predictions of R_{AA}^T for different centrality classes, based on the full-fledged DREENA-C framework, are consistent with the available experimental data. In Fig. 2 we compare our R_{AA}^T vs p_{\perp} predictions for charged hadrons with corresponding 5.02-TeV Pb + Pb LHC data from A Large Ion Collider Experiment (ALICE) [57], Compact Muon Solenoid

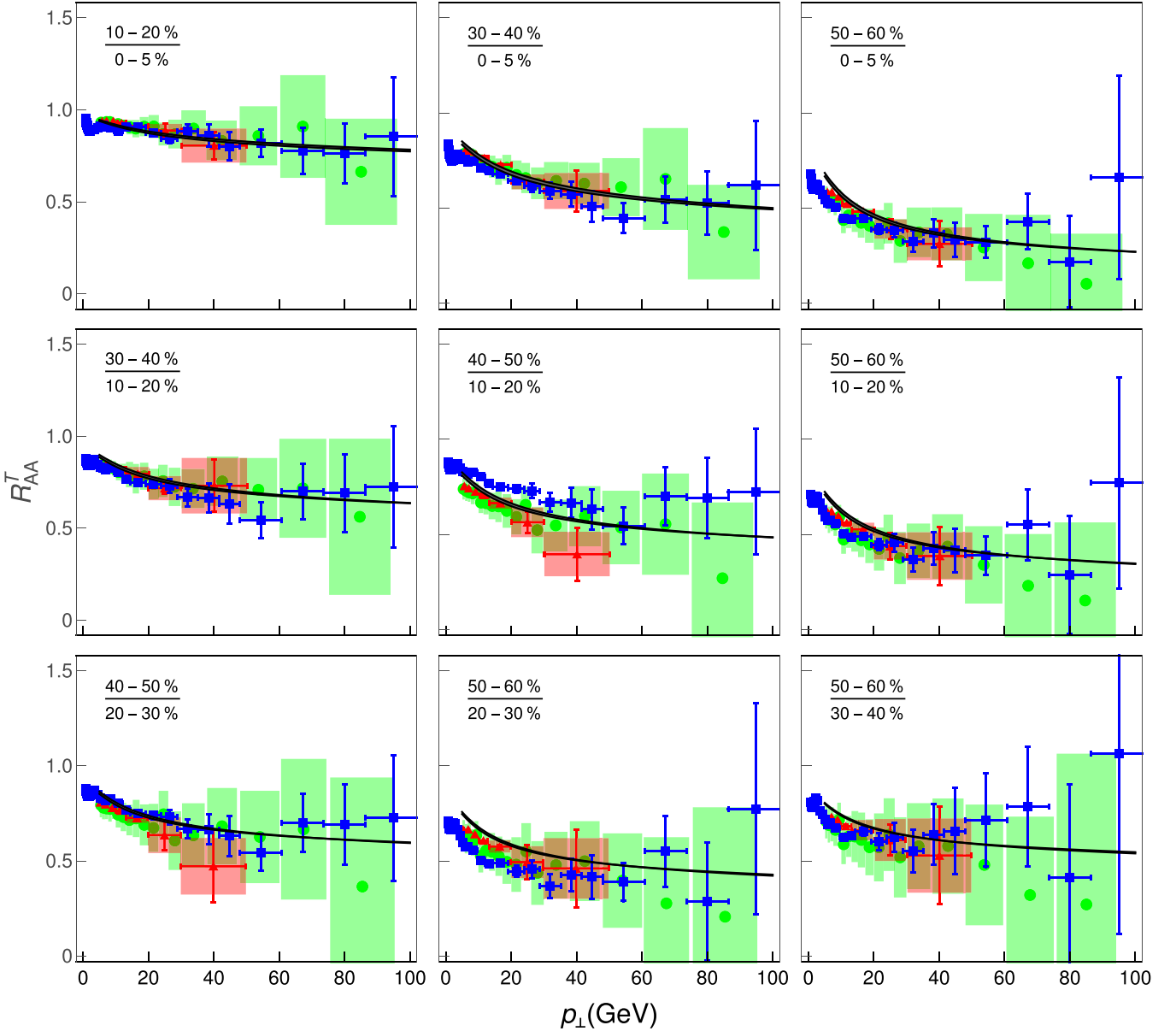


FIG. 2. Charged hadron R_{AA}^T for different pairs of centrality classes as a function of p_{\perp} . The predictions generated within our full-fledged suppression numerical procedure DREENA-C [28] (black curves with corresponding gray bands) are compared with ALICE [57] (red triangles), CMS [58] (blue squares), and ATLAS [59] (green circles) data. The lower (upper) boundary of each band corresponds to $\mu_M/\mu_E = 0.6$ ($\mu_M/\mu_E = 0.4$). Centrality pairs are indicated in the upper-left corner of each plot.

(CMS) [58], and A Toroidal LHC ApparatuS (ATLAS) [59], for different centrality pairs as indicated in the upper-left corner of each plot. Despite the large error bars, for all centrality pairs we observe consistency between our DREENA-C predictions and experimental data, in the p_{\perp} region where our formalism is applicable ($p_{\perp} \gtrsim 10$ GeV). Moreover, we also notice the flattening of each curve with increasing p_{\perp} (≈ 100 GeV), confirming that the expecting saturating (limiting) behavior is reached.

Furthermore, based on the analytical relation provided by Eq. (7), we expect linear functional dependence between $\ln R_{AA}^T$ and $\ln(T/T_{\text{ref}})$, which we test in Fig. 3. Note that all quantities throughout the paper are determined at $p_{\perp} = 100$ GeV, and by calculating R_{AA}^T for various centrality pairs

(see figure captions) within the full-fledged DREENA procedure. Remarkably, from Fig. 3, we observe that $\ln(R_{AA}^T)$ and $\ln(T/T_{\text{ref}})$ are indeed linearly related, which confirms the validity of our scaling arguments at high p_{\perp} and the proposed procedure.

Linear fit to calculated points in Fig. 3 leads to the proportionality factor $f = a + kb = 3.79 \approx 4$. This small value of f would lead to k smaller than 1 if (commonly assumed) $a = 3$ and $b = 2$ are used. Such k value seems, however, implausible, as it would require (T/T_{ref}) to change more slowly with centrality compared to (L/L_{ref}) .

More importantly, the temperature exponent can now be extracted ($b \approx 1.4$ as estimated in Ref. [26]), leading to $a \approx 1.2$. This indicates that temperature dependence of energetic

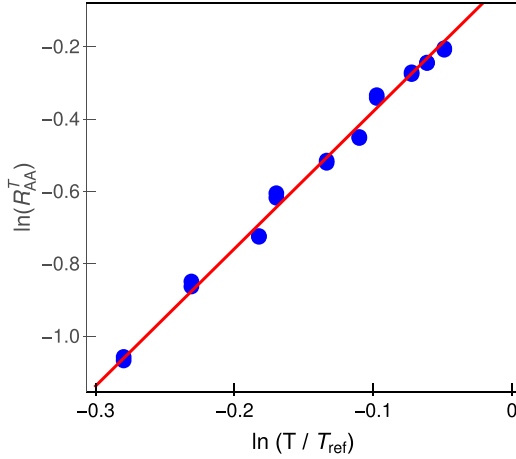


FIG. 3. $\ln(R_{AA}^T)$ vs $\ln(T/T_{\text{ref}})$ relation. $\ln(R_{AA}^T)$ and $\ln(T/T_{\text{ref}})$ are calculated from the full-fledged DREENA-C framework [28], for h^\pm at $p_\perp = 100$ GeV in 5.02-TeV Pb+Pb collisions at the LHC for different centrality pairs. The referent centrality values are 10–20, 20–30, 30–40, and 40–50%, while their counterpart values are always higher, with the highest being equal to 50–60%. The red solid line corresponds to the linear fit to the values. Remaining parameters are the same as in Fig. 2.

particle energy loss (at very high p_\perp) is close to linear (see Eq. (3)), that is, certainly not quadratic or cubic, as commonly considered. This is in accordance with previously reported dependence of fractional dynamical energy loss on T somewhere between linear and quadratic [29], and as opposed to commonly used pQCD estimate $a = 3$ for radiative [9–12,14–20] (or even $a = 2$ for collisional [7,21–23]) energy loss.

The extraction of T dependence, together with previously estimated path-length dependence [26], within the DREENA framework, allows utilizing this new observable R_{AA}^T in discriminating between energy-loss models, with the aim of better understanding QGP properties. To this end, in Fig. 4, we (i) test sensitivity of R_{AA}^T on different medium evolutions (constant temperature, 1D Bjorken [60], and full 3+1D hydrodynamics [61]) and (ii) compare the asymptote derived from this study $((T/T_{\text{ref}})^{1.2}(L/L_{\text{ref}})^{1.4})$, with the commonly used estimate of $(T/T_{\text{ref}})^3(L/L_{\text{ref}})^2$.

Several conclusions can be drawn from Fig. 4.

(i) With respect to different models of QGP expansion, we see that, as expected, obtained R_{AA}^T results are similar, i.e., not very sensitive to the details of the medium evolution. As in DREENA-C (and DREENA-B; see the next subsection) the temperature dependence can be analytically tracked (which is, however, not possible in more complex DREENA-A), this result additionally confirms that the DREENA-C framework is suitable for the extraction of energy-loss temperature dependence.

(ii) Ideally, the T dependence exponent could be directly extracted from experimental data, by fitting a straight line to the very high- p_\perp part (≈ 100 GeV) of R_{AA}^T for practically any centrality pair (upon L the dependence exponent is determined following Ref. [26]). However, the fact that data from different experiments (ALICE, CMS, and ATLAS) are not ideally consistent, and that the error bars are quite sizable,

currently prevents such direct extraction. The error bars in the upcoming high-luminosity third run at the LHC are, however, expected to significantly decrease, which would enable the direct extraction of the exponent a from the data.

(iii) Finally, Fig. 4 also indicates that widely considered energy-loss dependence T^3L^2 may be inconsistent with the experimental data. Future increase in measurements precision could provide confidence in this observation and resolve the exact form of these dependencies from the data, through our proposed observable. This discriminative power of the R_{AA}^T quantity highlights its importance in understanding the underlying energy-loss mechanisms in QGP.

A. Effects of medium evolution

While in Fig. 4 we showed that R_{AA}^T results are robust with respect to the medium evolution, the analytical procedure for extracting temperature dependence is different in DREENA-C and DREENA-B frameworks. A comparison of scaling factors extracted from these two procedures can be used to test reliability of the proposed procedure. In this subsection, we consequently utilize the DREENA-B framework [27], where medium evolution is introduced through Bjorken 1D hydrodynamical expansion [60], i.e., there is the following functional dependence of T on path length:

$$T = T_0 \left(\frac{\tau_0}{l} \right)^{1/3}, \quad (9)$$

where T_0 and $\tau_0 = 0.6$ fm [62,63] denote initial temperature and thermalization time of the QGP.

Proceeding in a similar manner as in constant medium case, R_{AA}^T (given by Eq. (4)) in the evolving medium (for coupled local T and l , where l stands for traversed path length) reads

$$\begin{aligned} R_{AA}^T &= \frac{\int_0^L T^a l^{b-1} dl}{\int_0^{L_{\text{ref}}} (T_{\text{ref}})^a (l_{\text{ref}})^{b-1} dl_{\text{ref}}} = \frac{T_0^a \tau_0^{a/3} \int_0^L \frac{l^{b-1}}{l^{a/3}} dl}{T_{0,\text{ref}}^a \tau_0^{a/3} \int_0^{L_{\text{ref}}} \frac{(l_{\text{ref}})^{b-1}}{(l_{\text{ref}})^{a/3}} dl_{\text{ref}}} \\ &= \left(\frac{T_0}{T_{0,\text{ref}}} \right)^a \left(\frac{L}{L_{\text{ref}}} \right)^{b-\frac{a}{3}}, \end{aligned} \quad (10)$$

where we used Eq. (9). Again, we assess whether there is a simple relation between logarithms of the (now initial) temperature ratio and average path-length ratio for different centrality pairs. Similarly to the constant T case, from Fig. 5 we infer linear dependence between these two quantities, where the slope coefficient now acquires the value $\kappa \approx 1.3$. Thus, we may write

$$\frac{L}{L_{\text{ref}}} = \left(\frac{T_0}{T_{0,\text{ref}}} \right)^\kappa \Rightarrow \frac{T_0}{T_{0,\text{ref}}} = \left(\frac{L}{L_{\text{ref}}} \right)^{1/\kappa}, \quad (11)$$

which ensures that the R_{AA}^T quantity has a very simple form, depending only on average path length and exponents a , b , and κ :

$$R_{AA}^T = \left(\frac{L}{L_{\text{ref}}} \right)^{\frac{a}{\kappa} + b - \frac{a}{3}}. \quad (12)$$

If we substitute the value of $a \approx 1.2$ obtained in the constant T medium case, previously estimated $b \approx 1.4$ [26], and

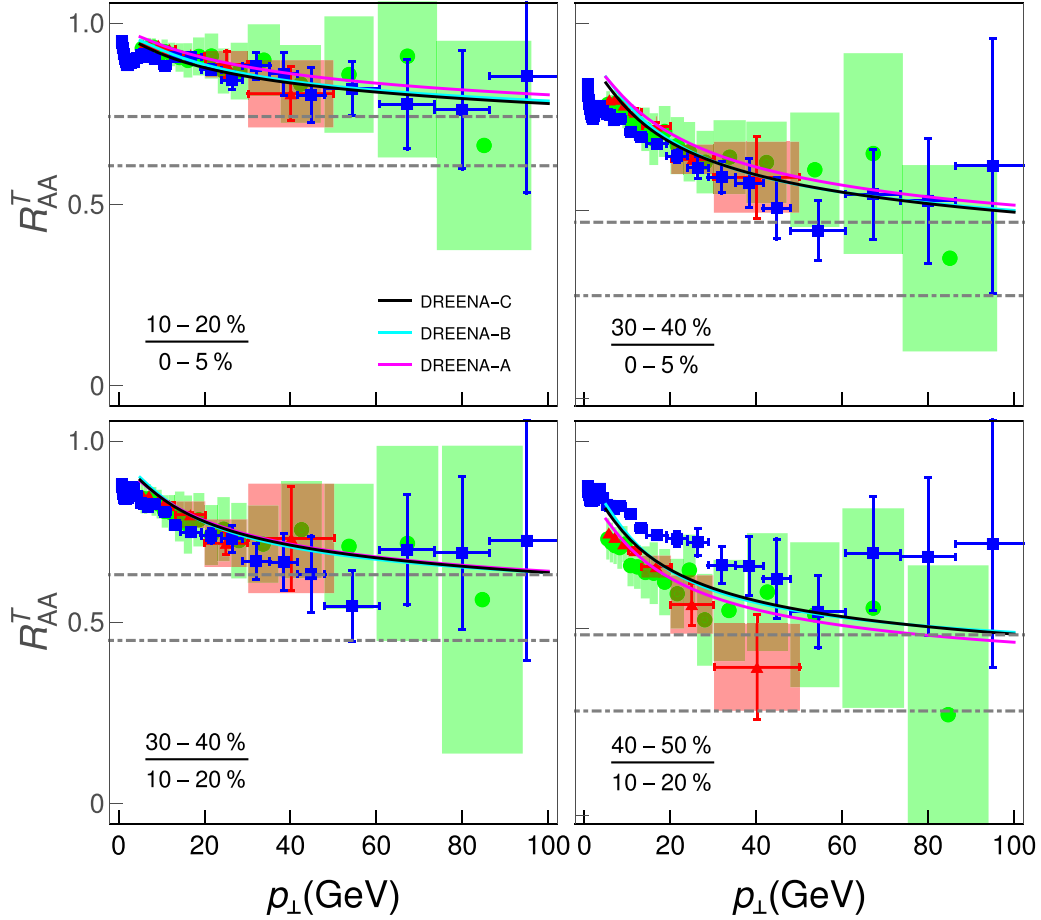


FIG. 4. The discriminative power of the R_{AA}^T quantity in resolving the energy-loss mechanism. Four panels in Fig. 2 are extended to include comparison of our asymptotic scaling behavior $(T/T_{\text{ref}})^{1.2}(L/L_{\text{ref}})^{1.4}$ (gray dashed horizontal line) with common assumption $(T/T_{\text{ref}})^3(L/L_{\text{ref}})^2$ (gray dot-dashed horizontal line). The figure also shows comparison of R_{AA}^T s obtained by three different numerical frameworks: constant temperature DREENA-C (black curve), 1D Bjorken expansion DREENA-B [27] (cyan curve), and full 3+1D hydrodynamics evolution [61] DREENA-A (magenta curve). The remaining labeling is the same as in Fig. 2.

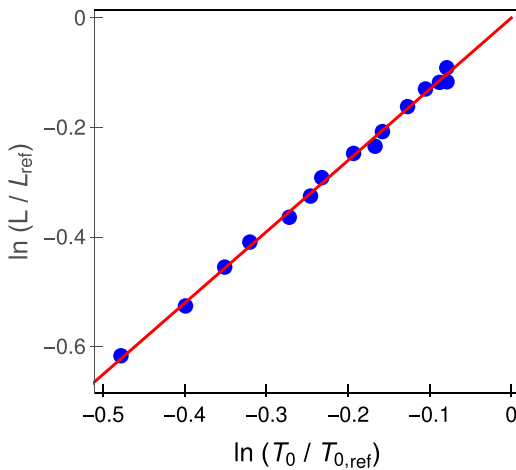


FIG. 5. $\ln(L/L_{\text{ref}})$ vs $\ln(T_0/T_{0,\text{ref}})$ for various pairs of centralities in evolving medium. The assumed centrality pairs are the same as in Fig. 1. The red solid line corresponds to the linear fit to the values.

here inferred $\kappa \approx 1.3$, we arrive at the following estimate:

$$R_{AA}^T = \left(\frac{L}{L_{\text{ref}}}\right)^{1.93} \Rightarrow \ln(R_{AA}^T) = 1.93 \ln\left(\frac{L}{L_{\text{ref}}}\right). \quad (13)$$

This equation is quite suitable for testing the robustness of the procedure for extracting the exponent a to inclusion of the evolving medium. Namely, value 1.93 in Eq. (13) stems from coefficient a , which is extracted from the constant T medium case. On the other hand, if we plot $\ln(R_{AA}^T)$, generated by full-fledged DREENA-B calculations (i.e., in the evolving medium) which are *fundamentally different* from DREENA-C, against $\ln(L/L_{\text{ref}})$ for a variety of centrality pairs, again we observe a linear dependence (see Fig. 6). Furthermore, a linear fit to the values surprisingly yields the exact same slope coefficient value of 1.93 (see also Table I).

Consequently, the procedure of extracting the temperature-dependence exponent, introduced first in the case of the constant T medium, is applicable to the expanding medium as well. Moreover, the fact that the same coefficient a is obtained through two different procedures leads us to conclude that (i) for the purpose of this paper the DREENA-C framework

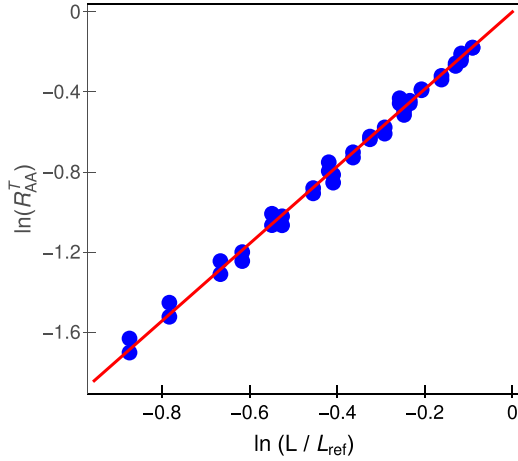


FIG. 6. Testing the validity of our procedure for temperature-dependence extraction in the case of the expanding QCD medium. $\ln(R_{AA}^T)$ vs $\ln(L/L_{\text{ref}})$ for h^\pm at $p_\perp = 100$ GeV for different pairs of centrality classes is plotted. Suppression predictions are obtained from full-fledged DREENA-B [27] calculations. Referent centrality values are 5–10, 10–20, 20–30, 30–40, 40–50, and 50–60%, while their counterpart values are always higher, with the highest being 60–70%. The red solid line corresponds to the linear fit to the values.

(assuming a constant temperature medium) is sufficient and (ii) the same energy-loss scaling holds in an evolving medium (i.e., for local temperature) as well. The displayed consistency of the results provides confidence in the general applicability of our procedure (suggesting robustness to the applied model of the bulk medium) and supports the reliability of the value of extracted T dependence exponent $a \approx 1.2$.

It is worth noting that the definition of R_{AA}^T relies on the fact that we assume that $R_{AA} = 1$ if no energy loss is encountered. Related to this, we do not study the effect of (nuclear) parton distribution function differences on R_{AA} , as it is generally studied under initial-state effects. However, it is known that initial-state effects have a sizable impact only on the low- and moderate- p_\perp sector (lower than 6 GeV) [64–70]. Since our numerical predictions are generated above 8–10 GeV and the temperature dependence is extracted at very high- p_\perp values ($p_\perp \sim 100$ GeV), these effects will be negligible in this p_\perp region, and should not influence the results obtained in our paper.

B. Effects of colliding system size

We below extend our analysis to smaller colliding systems in order to assess generality of the conclusions presented

TABLE I. Inferred temperature-dependence exponent across different frameworks.

Framework	Temperature dependence exponent
DREENA-C	$a \approx 1.2$
DREENA-B	Consistent with $a \approx 1.2$
DREENA-A	Not analytically tractable

above. Smaller colliding systems, such as Xe + Xe, Kr + Kr, Ar + Ar, and O + O, are important to gradually resolve the issue of QGP formation in small systems (such as pA), and (except Xe + Xe, which is already in a run) are expected to be a part of the future heavy-ion program at the LHC [71].

As already discussed in Ref. [26], for this analysis within the DREENA-C framework [28] (which we employ here for simplicity, since the robustness of the procedure to the evolving medium was demonstrated above) note that R_{AA} depends on (i) initial high- p_\perp parton distribution, (ii) medium average T , and (iii) path-length distribution. For different colliding systems (probably at slightly different $\sqrt{s_{NN}} = 5.44$ TeV compared to the Pb + Pb system) we employ the same high- p_\perp distributions, since in Ref. [29] it was shown that for almost twofold increase of the collision energy (from 2.76 to 5.02 TeV) the change in corresponding initial distributions results in a negligible change (approximately 5%) in suppression.

Regarding the average temperature, one should note that T is directly proportional to the charged particle multiplicity, while inversely proportional to the size of the overlap area and average medium size [26,28,47,48], i.e., $T \propto (\frac{dN_{ch}/d\eta}{A_\perp L})^{1/3}$. The transition to smaller colliding systems, for a certain fixed centrality class, leads to the following scaling: $A_\perp \propto A^{2/3}$, $L \propto A^{1/3}$ [72,73], and $dN_{ch}/d\eta \propto N_{\text{part}} \propto A$ [74,75], where A denotes atomic mass. This leads to $T \sim (\frac{A}{A_\perp^3 L^3})^{1/3} \sim \text{const}$, that is, we expect that average temperature does not change, when transitioning from large Pb + Pb to smaller systems, for a fixed centrality class. Lastly, path-length distributions for smaller systems and each centrality class are obtained in the same manner as for Pb+Pb [28], and are the same as in Pb + Pb collisions up to a rescaling factor of $A^{1/3}$.

By denoting all quantities related to smaller systems with a tilde, with Pb + Pb quantities denoted as before, it is straightforward to show that the temperature sensitive suppression ratio for smaller systems satisfies

$$\begin{aligned} \tilde{R}_{AA}^T &= \frac{1 - \tilde{R}_{AA}}{1 - R_{AA}^{\text{ref}}} \approx \frac{\tilde{T}^a \tilde{L}^b}{T_{\text{ref}}^a L_{\text{ref}}^b} \approx \frac{T^a L^b (\tilde{A}/A)^{b/3}}{T_{\text{ref}}^a L_{\text{ref}}^b (\tilde{A}/A)^{b/3}} \\ &= \frac{1 - R_{AA}}{1 - R_{AA}^{\text{ref}}} = R_{AA}^T, \end{aligned} \quad (14)$$

where we used $\tilde{T} = T$ and $\tilde{L}/L = (\tilde{A}/A)^{1/3}$.

To validate equality of R_{AA}^T s for different system sizes, predicted by analytical scaling behavior (Eq. (14)), in Fig. 7 we compare our full-fledged R_{AA}^T predictions for h^\pm in the Pb + Pb system with those for smaller colliding systems. We observe that, practically irrespective of system size, R_{AA}^T exhibits the same asymptotical behavior at high p_\perp . This not only validates our scaling arguments, but also demonstrates the robustness of the new observable R_{AA}^T to system size. Consequently, since for fixed centrality range T should remain the same for all these colliding systems, we obtained that temperature-dependence exponent a should be the same independently of the considered colliding system (see Fig. 3). Therefore, the proposed procedure for extracting the

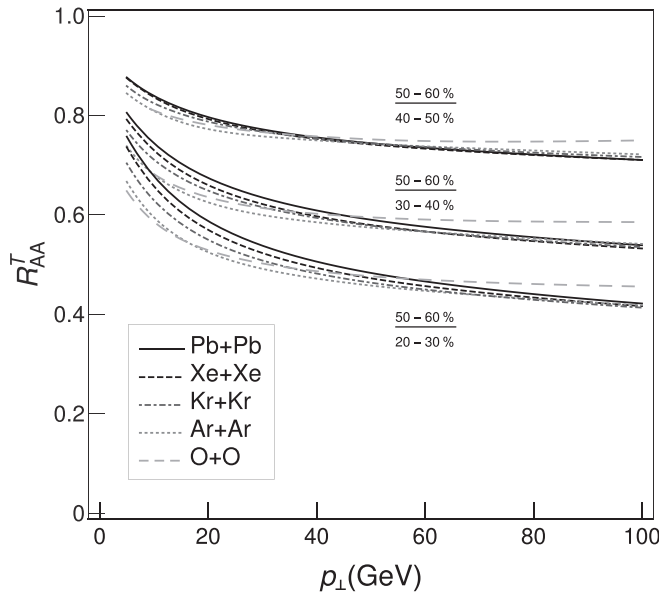


FIG. 7. Dependence of R_{AA}^T on a system size as a function of p_{\perp} . Predictions for h^{\pm} generated within the full-fledged DREENA-C [28] suppression numerical procedure are compared for different colliding systems: Pb+Pb, Xe + Xe, Kr + Kr, Ar + Ar, and O + O (for lines specification see legend). For clarity, the results are shown only for three centrality pairs, as specified in the plot, although checked for all available centrality classes. The magnetic to electric mass ratio is fixed to $\mu_M/\mu_E = 0.4$.

temperature dependence of the energy loss is also robust to the collision system size. As a small exception, the O + O system exhibits a slight departure from the remaining systems at high p_{\perp} , which might be a consequence of the fact that this system is significantly smaller than other systems considered here.

V. CONCLUSIONS AND OUTLOOK

One of the main signatures of the high- p_{\perp} particle's energy loss, apart from its path length, is its temperature dependence. Although extensive studies on both issues were performed, not until recently was the path-length dependence resolution suggested [26]. Here we proposed a new simple observable for extracting temperature dependence of the energy loss, based on one of the most common jet quenching observables—the high- p_{\perp} suppression. By combining full-fledged numerical calculations with asymptotic scaling behavior, we surprisingly obtained that temperature dependence is nearly linear, i.e., far from quadratic or cubic, as commonly assumed. Further, we verified its robustness and reliability on colliding system size and evolving QGP medium. Moreover, we demonstrated that the same observable, due to its joint dependence on T and L exponents, can be utilized to discriminate between different energy-loss models on *both* their *temperature* and *path-length* dependence bases. Comparison with the experimental data also indicated a need for revising the long-standing $\Delta E/E \propto L^2 T^3$ paradigm.

As an outlook, the expected substantial decrease of error bars in the upcoming third run measurements at the LHC will allow direct extraction of the temperature-dependence exponent from high- p_{\perp} data of this observable. This will provide a resolving power to temperature/path-length [26] dependence of the energy loss and test our understanding of the underlying QGP physics.

ACKNOWLEDGMENTS

We thank Pasi Huovinen and Jussi Auvinen for useful discussions. This work is supported by the European Research Council (Grant No. ERC-2016-COG: 725741), and by the Ministry of Science and Technological Development of the Republic of Serbia (Projects No. ON171004 and No. ON173052).

- [1] M. Gyulassy and L. McLerran, *Nucl. Phys. A* **750**, 30 (2005).
- [2] E. V. Shuryak, *Nucl. Phys. A* **750**, 64 (2005).
- [3] C. V. Johnson and P. Steinberg, *Phys. Today* **63**(5), 29 (2010).
- [4] B. Jacak and P. Steinberg, *Phys. Today* **63**(5), 39 (2010).
- [5] J. C. Collins and M. J. Perry, *Phys. Rev. Lett.* **34**, 1353 (1975).
- [6] G. Baym and S. A. Chin, *Phys. Lett. B* **62**, 241 (1976).
- [7] J. D. Bjorken, FERMILAB-PUB-82-059-THY, 287 (1982).
- [8] J. Adams *et al.* (STAR Collaboration), *Phys. Rev. Lett.* **91**, 072304 (2003); C. Adler *et al.* (STAR Collaboration), *ibid.* **90**, 082302 (2003).
- [9] R. Baier, Y. Dokshitzer, A. Mueller, S. Peigne, and D. Schiff, *Nucl. Phys. B* **484**, 265 (1997).
- [10] N. Armesto, C. A. Salgado, and U. A. Wiedemann, *Phys. Rev. D* **69**, 114003 (2004).
- [11] C. A. Salgado and U. A. Wiedemann, *Phys. Rev. D* **68**, 014008 (2003).
- [12] M. Gyulassy, P. Levai, and I. Vitev, *Nucl. Phys. B* **594**, 371 (2001).
- [13] B. G. Zakharov, *JETP Lett.* **70**, 176 (1999); **73**, 49 (2001).
- [14] P. B. Arnold, G. D. Moore, and L. G. Yaffe, *J. High Energy Phys.* **06** (2002) 030.
- [15] X. N. Wang and X. F. Guo, *Nucl. Phys. A* **696**, 788 (2001).
- [16] C. Andres, N. Armesto, M. Luzum, C. A. Salgado, and P. Zurita, *Eur. Phys. J. C* **76**, 475 (2016).
- [17] B. Betz and M. Gyulassy, *Phys. Rev. C* **86**, 024903 (2012).
- [18] B. Betz and M. Gyulassy, *J. High Energy Phys.* **08** (2014) 090; **10** (2014) 043.
- [19] J. Noronha-Hostler, B. Betz, J. Noronha, and M. Gyulassy, *Phys. Rev. Lett.* **116**, 252301 (2016).
- [20] A. Majumder and C. Shen, *Phys. Rev. Lett.* **109**, 202301 (2012).
- [21] M. H. Thoma and M. Gyulassy, *Nucl. Phys. B* **351**, 491 (1991).
- [22] E. Braaten and M. H. Thoma, *Phys. Rev. D* **44**, 1298 (1991); **44**, 2625(R) (1991).
- [23] Y. He, T. Luo, X.-N. Wang, and Y. Zhu, *Phys. Rev. C* **91**, 054908 (2015); **97**, 019902(E) (2018).
- [24] C. Nonaka and S. A. Bass, *Phys. Rev. C* **75**, 014902 (2007).
- [25] C. Marquet and T. Renk, *Phys. Lett. B* **685**, 270 (2010).
- [26] M. Djordjevic, D. Zigic, M. Djordjevic, and J. Auvinen, *Phys. Rev. C* **99**, 061902(R) (2019).

- [27] D. Zigic, I. Salom, M. Djordjevic, and M. Djordjevic, *Phys. Lett. B* **791**, 236 (2019).
- [28] D. Zigic, I. Salom, J. Auvinen, M. Djordjevic, and M. Djordjevic, *J. Phys. G* **46**, 085101 (2019).
- [29] M. Djordjevic and M. Djordjevic, *Phys. Rev. C* **92**, 024918 (2015).
- [30] M. Djordjevic, *Phys. Rev. C* **80**, 064909 (2009).
- [31] M. Djordjevic and U. Heinz, *Phys. Rev. Lett.* **101**, 022302 (2008).
- [32] M. Djordjevic, *Phys. Rev. C* **74**, 064907 (2006).
- [33] J. I. Kapusta, *Finite-Temperature Field Theory* (Cambridge University, Cambridge, England, 1989).
- [34] M. Djordjevic and M. Gyulassy, *Nucl. Phys. A* **733**, 265 (2004).
- [35] M. Djordjevic, *Phys. Lett. B* **709**, 229 (2012).
- [36] M. Djordjevic and M. Djordjevic, *Phys. Lett. B* **734**, 286 (2014).
- [37] B. Blagojevic, M. Djordjevic, and M. Djordjevic, *Phys. Rev. C* **99**, 024901 (2019).
- [38] A. Peshier, [arXiv:hep-ph/0601119](https://arxiv.org/abs/hep-ph/0601119).
- [39] R. Field, *Applications of Perturbative QCD* (Perseus, Cambridge, MA, 1995).
- [40] M. Djordjevic and M. Gyulassy, *Phys. Rev. C* **68**, 034914 (2003).
- [41] B. Blagojevic and M. Djordjevic, *J. Phys. G* **42**, 075105 (2015).
- [42] Z. B. Kang, I. Vitev, and H. Xing, *Phys. Lett. B* **718**, 482 (2012); R. Sharma, I. Vitev, and B. W. Zhang, *Phys. Rev. C* **80**, 054902 (2009).
- [43] M. Gyulassy, P. Levai, and I. Vitev, *Phys. Lett. B* **538**, 282 (2002).
- [44] S. Wicks, W. Horowitz, M. Djordjevic, and M. Gyulassy, *Nucl. Phys. A* **784**, 426 (2007).
- [45] A. Dainese, *Eur. Phys. J. C* **33**, 495 (2004).
- [46] D. de Florian, R. Sassot, and M. Stratmann, *Phys. Rev. D* **75**, 114010 (2007).
- [47] M. Djordjevic, M. Djordjevic, and B. Blagojevic, *Phys. Lett. B* **737**, 298 (2014).
- [48] J. Xu, A. Buzzatti, and M. Gyulassy, *J. High Energy Phys.* **08** (2014) 063.
- [49] J. Adam *et al.* (ALICE Collaboration), *Phys. Rev. Lett.* **116**, 222302 (2016).
- [50] J. Adam *et al.* (ALICE Collaboration), *Phys. Lett. B* **754**, 235 (2016); M. Wilde (for the ALICE Collaboration), *Nucl. Phys. A* **904-905**, 573c (2013).
- [51] M. Djordjevic, M. Gyulassy, R. Vogt, and S. Wicks, *Phys. Lett. B* **632**, 81 (2006).
- [52] A. Bazavov *et al.* (HotQCD Collaboration), *Phys. Rev. D* **90**, 094503 (2014).
- [53] Y. Maenzawa, S. Aoki, S. Ejiri, T. Hatsuda, N. Ishii, K. Kanaya, N. Ukita, and T. Umeda (WHOT-QCD Collaboration), *Phys. Rev. D* **81**, 091501(R) (2010).
- [54] A. Nakamura, T. Saito, and S. Sakai, *Phys. Rev. D* **69**, 014506 (2004).
- [55] T. Renk, *Phys. Rev. C* **85**, 044903 (2012).
- [56] D. Molnar and D. Sun, *Nucl. Phys. A* **932**, 140 (2014); **910-911**, 486 (2013).
- [57] S. Acharya *et al.* (ALICE Collaboration), *J. High Energy Phys.* **11** (2018) 013.
- [58] V. Khachatryan *et al.* (CMS Collaboration), *J. High Energy Phys.* **04** (2017) 039.
- [59] (ATLAS Collaboration), ATLAS-CONF-2017-012 (2017).
- [60] J. D. Bjorken, *Phys. Rev. D* **27**, 140 (1983).
- [61] E. Molnar, H. Holopainen, P. Huovinen, and H. Niemi, *Phys. Rev. C* **90**, 044904 (2014).
- [62] P. F. Kolb and U. W. Heinz, Hydrodynamic description of ultra-relativistic heavy ion collisions, in *Quark-Gluon Plasma*, edited by R. C. Hwa and X.-N. Wang (World Scientific, Singapore, 2004), Vol. 3, p. 634.
- [63] J. E. Bernhard, J. S. Moreland, and S. A. Bass, *Nucl. Phys. A* **967**, 293 (2017).
- [64] M. R. Adams *et al.*, *Phys. Rev. Lett.* **68**, 3266 (1992).
- [65] V. Barone and M. Genovese, *Phys. Lett. B* **412**, 143 (1997).
- [66] A. Dainese (ALICE Collaboration), *Czech. J. Phys.* **55**, B367 (2005).
- [67] S. Cao, G.-Y. Qin, and S. A. Bass, *Phys. Rev. C* **92**, 024907 (2015).
- [68] J. W. Cronin, H. J. Frisch, M. J. Shochet, J. P. Boymond, P. A. Piroue, and R. L. Sumner, *Phys. Rev. D* **11**, 3105 (1975).
- [69] M. Lev and B. Petersson, *Z. Phys. C* **21**, 155 (1983).
- [70] A. Krzywicki, J. Engels, B. Petersson, and U. Sukhatme, *Phys. Lett. B* **85**, 407 (1979).
- [71] Z. Citron, A. Dainese, J. F. Grosse-Oetringhaus, J. M. Jowett, Y. J. Lee, U. A. Wiedemann, M. Winn, A. Andronic, F. Bellini, and E. Bruna, *CERN Yellow Rep. Monogr.* **7**, 1159 (2019).
- [72] G. Giacalone, J. Noronha-Hostler, M. Luzum, and J. Y. Ollitrault, *Phys. Rev. C* **97**, 034904 (2018).
- [73] C. Loizides, J. Kamin, and D. d'Enterria, *Phys. Rev. C* **97**, 054910 (2018).
- [74] K. J. Eskola, H. Niemi, R. Paatelainen, and K. Tuominen, *Phys. Rev. C* **97**, 034911 (2018).
- [75] S. Acharya *et al.* (ALICE Collaboration), *Phys. Lett. B* **790**, 35 (2019).

Understanding Infection Progression under Strong Control Measures through Universal COVID-19 Growth Signatures

Magdalena Djordjevic,* Marko Djordjevic,* Bojana Ilic, Stefan Stojku, and Igor Salom

Widespread growth signatures in COVID-19 confirmed case counts are reported, with sharp transitions between three distinct dynamical regimes (exponential, superlinear, and sublinear). Through analytical and numerical analysis, a novel framework is developed that exploits information in these signatures. An approach well known to physics is applied, where one looks for common dynamical features, independently from differences in other factors. These features and associated scaling laws are used as a powerful tool to pinpoint regions where analytical derivations are effective, get an insight into qualitative changes of the disease progression, and infer the key infection parameters. The developed framework for joint analytical and numerical analysis of empirically observed COVID-19 growth patterns can lead to a fundamental understanding of infection progression under strong control measures, applicable to outbursts of both COVID-19 and other infectious diseases.

COVID-19 pandemic introduced unprecedented worldwide social distancing measures.^[1] While interventions such as quarantine or vaccination have been extensively studied in quantitative epidemiology, effects of social distancing are not well understood,^[2–4] and when addressed, they have been studied only numerically. Unique opportunity to understand these effects has been provided by COVID-19 tracing through confirmed case counts, active cases and fatalities, in a variety of countries with different demographic and environmental conditions.^[5,6] We here show that focusing on analytical and numerical derivations in distinct epidemics growth regimes, is

a novel and effective approach in revealing infection progression mechanisms that may be a valuable alternative to detailed numerical simulations.


We start by introducing our COVID-19 dynamics model. We then extract COVID-19 count data^[7] and select those countries that systematically trace not only confirmed cases and fatalities, but also active cases (Andorra, Austria, Czechia, Croatia, Cuba, Germany, Israel, New Zealand, Switzerland and Turkey), which allows tight constraint of numerical analysis. We observe three characteristic growth regimes in confirmed case counts, show that our model is well constrained by these regimes for a wide range of countries, and provide an intuitive explanation behind the emergence of such regimes. Our analytical results

for the characteristic (inflection and maximum) points of the infective curve will allow to i) explain the nearly constant value of the scaling exponent in the superlinear regime of confirmed counts; ii) understand the relation between the duration of this regime and strength of social distancing; iii) pinpoint changes in the reproduction number from outburst to extinguishing the infection, and iv) constrain the main parameter quantifying the effect of social distancing by analyzing scaling of the infection growth with time in the sub-linear regime. The obtained constraints provide a basis for successful analysis of countries that did not continuously track the active cases (here demonstrated for France, Italy, Spain, United Kingdom, and Serbia). We will finally present the key infection parameters inferred through combined analytical and numerical analysis.

We develop a mechanistic model (nonlinear and nonhomogeneous), which takes into account gradual introduction of social distancing (as relevant for most countries' response), in addition to other important infection progression mechanisms. We start from standard compartments for epidemiological models, that is, susceptible (S), exposed (E), infective (I), and recovered (R).^[2–4] To account for social distancing and observable quantities, we introduce additional compartments: protected (P)—where individuals effectively move from susceptible category due to social distancing; total number of diagnosed (confirmed and consequently quarantined) cases (D), active cases (A), and fatalities (F). D , A , and F correspond to directly observable (measured) quantities, but are indirect observables of I , as only part of infective individuals gets diagnosed, due to a large number of mild/asymptomatic cases.^[8]

Dr. M. Djordjevic, Dr. B. Ilic, S. Stojku, Dr. I. Salom
Institute of Physics Belgrade
University of Belgrade
Belgrade 11080, Serbia
E-mail: magda@ipb.ac.rs

Prof. M. Djordjevic
Quantitative Biology Group
Faculty of Biology
University of Belgrade
Belgrade 11000, Serbia
E-mail: dmarko@bio.bg.ac.rs

 The ORCID identification number(s) for the author(s) of this article can be found under <https://doi.org/10.1002/gch2.202000101>.

© 2021 The Authors. *Global Challenges* published by Wiley-VCH GmbH. This is an open access article under the terms of the Creative Commons Attribution License, which permits use, distribution and reproduction in any medium, provided the original work is properly cited.

DOI: 10.1002/gch2.202000101

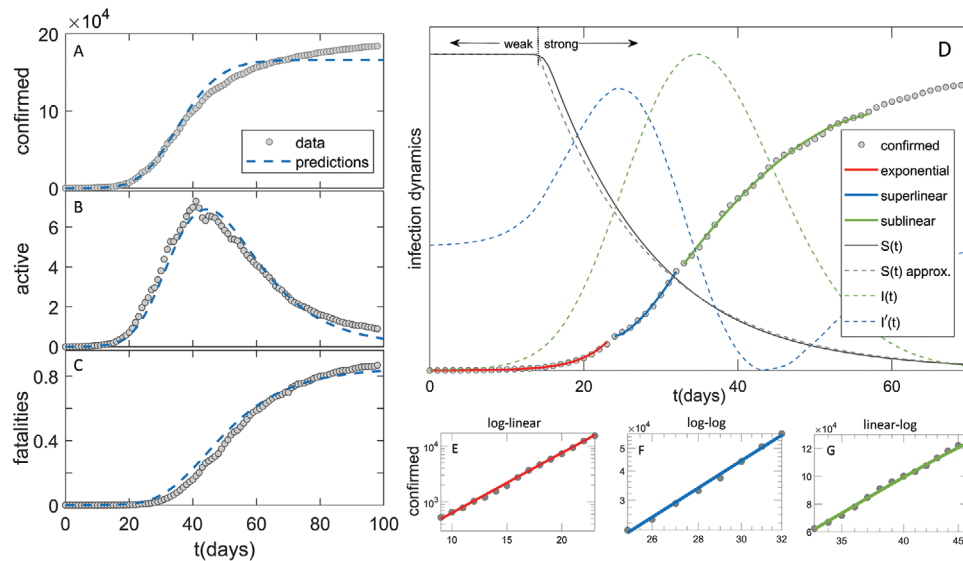


Figure 1. Comparison of the model (dashed blue curves) with the data in the case of Germany (grey circles) for A) confirmed case counts, B) active cases, C) fatalities. D) Exponential, superlinear, and sublinear fit to confirmed case data, is shown. Arrows “weak” and “strong” indicate, respectively, the regions with a small and large magnitude of social distancing. The full grey curve denotes susceptibles ($S(t)$), where the dashed grey curve shows an approximation to $S(t)$. The dashed green curve denotes the number of infectious cases ($I(t)$), where the dashed blue curve is $I'(t)$, whose maxima indicate $I(t)$ inflection points. The confirmed case counts in the three regimes are shown on E) log-linear, F) log-log and G) linear-log scale.

We implement the model deterministically, as COVID-19 count numbers are very high wherever reasonable testing capacities are employed. This makes model analytically tractable, and allows robust parameter inference through combination of analytically derived expressions and tightly constrained numerical analysis, as we show below. Our analysis is applied separately to each country, as the effect of social distancing, initial numbers of infected and exposed cases, diagnosis/detection efficiency and transmission rates may be different. However, within a given country, we do not take into account different heterogeneities—demographic, spatial, population activity, or seasonality effects.^[2,9,10] Alternatively, global dynamical properties of the outbreak can be analyzed in a probabilistic framework employing partial differential equations in an age-structured model.^[11,12] These can readily be included in our model, but would lead to model structure which is not analytically tractable, so these extensions are left for future work.

Given this, the model equations are:

$$dS/dt = -\beta IS/N - dP/dt; \quad dP/dt = \alpha/(1+(t_0/t)^n)S \quad (1)$$

$$dE/dt = \beta IS/N - \sigma E; \quad dI/dt = \sigma E - \gamma I - \varepsilon \delta I; \quad dR/dt = \gamma I \quad (2)$$

$$dD/dt = \varepsilon \delta I; \quad dA/dt = \varepsilon \delta I - hA - mA; \quad dF/dt = mA \quad (3)$$

where N is the total population number; β —the transmission rate; σ —inverse of the latency period; γ —inverse of the infectious period; δ —inverse of the detection/diagnosis period; ε —detection efficiency; h —the recovery rate; m —the mortality rate. Social distancing is included through Equation (1) (second equation), which represents the rate at which the

population moves (on average) from susceptible to protected category. The term $\frac{\alpha}{1+(t_0/t)^n}$ corresponds to a sigmoidal dependence

(similar to Fermi–Dirac function, in quantitative biology known as the Hill function^[13]). Time t_0 determines the half-saturation, so that well before t_0 the social distancing is negligible, while well after t_0 the rate of transition to the protected category approaches α . Parameter n (the Hill constant) determines how rapidly the social distancing is introduced, that is, large n leads to rapid transition from OFF to ON state, and vice versa.^[13] Equation (3) considers that only a fraction of the infected is diagnosed, so that $\varepsilon \delta I$ takes into account the diagnosis and the subsequent quarantine process.

To make the problem analytically tractable, we approximate the Hill function in the first relation of Equation (1) by unit step function, so that after t_0 the second term in Equation (1) becomes $-\alpha S$ and dominates over the first term, that is, $S(t) \approx e^{-\alpha t}$. We checked that this approximation agrees well with full-fledged numerical simulations (Figure 1D and Supporting Information). In all comparisons with analytical results, numerical analysis is done with the full model, allowing an independent check of both analytical derivations and employed approximations. Under this assumption, Equations (1) and (2) reduce to:

$$\frac{d^2 I(t)}{dt^2} + (\gamma + \varepsilon \delta + \sigma) \frac{dI(t)}{dt} = \sigma \{ \beta [\theta(t_0 - t) + e^{-(t-t_0)\alpha} \theta(t - t_0)] - (\gamma + \varepsilon \delta) \} I(t) \quad (4)$$

We next introduce two time regions: I) $t \leq t_0$ and II) $t > t_0$ and solve Equations (4) separately within these regions, where corresponding solutions are denoted as $I_I(t)$ and $I_{II}(t)$. As in the above expressions $\gamma + \varepsilon \delta$ always appear together, we further denote $\gamma + \varepsilon \delta \rightarrow \gamma$.

For $I_1(t)$, we take $I(t=0) \equiv I_0$, and restrict to dominant (positive) Jacobian eigenvalue, leading to the exponential regime:

$$I_1(t) = I_0 e^{2t \frac{1}{1-(\gamma+\sigma)+\sqrt{(\gamma-\sigma)^2+4\beta\sigma}}} \quad (5)$$

By shifting $t-t_0 \rightarrow t$, $I_{II}(t)$ is determined by

$$\frac{d^2 I_{II}(t)}{dt^2} + (\gamma + \sigma) \frac{dI_{II}(t)}{dt} = \sigma(\beta e^{-\alpha t} - \gamma) I_{II}(t) \quad (6)$$

Equation (6) is highly nontrivial, due to variable coefficient ($\sigma\beta e^{-\alpha t}$). By substituting variable $t \rightarrow x = \frac{-2i\sqrt{\beta\sigma}}{\alpha} e^{-\frac{\alpha t}{2}}$ it can be shown that Equation (6) reduces to transformed form of Bessel differential equation:^[14]

$$x^2 \frac{d^2 \gamma}{dx^2} + (1-2\alpha_1)x \frac{d\gamma}{dx} + (\beta_1^2 \gamma_1^2 x^{2\gamma_1} + \alpha_1^2 - v^2 \gamma_1^2) \gamma = 0 \quad (7)$$

whose general solution for noninteger v is given by:

$$\gamma(x) = x^{\alpha} [C_1 J(v, \beta_1 x^{\gamma_1}) + C_2 J(-v, \beta_1 x^{\gamma_1})] \quad (8)$$

where $J(v, x)$ represents Bessel function of the first kind, and C_1, C_2 are arbitrary constants. In our case $\alpha_1 = \frac{\gamma+\sigma}{\alpha}$, $\gamma_1 = \beta_1 = 1$, while $v = \frac{\gamma-\sigma}{\alpha}$ is indeed noninteger. If we return to t variable, taking into account the following relation between standard and modified ($I(v, x)$) Bessel functions of the first kind:^[15,16] $I(v, x) = i^{-v} J(v, ix)$, the general solution of Equation (6) reads:

$$I_{II}(t) = \left(\frac{\beta\sigma}{\alpha^2} e^{-\alpha t}\right)^{\frac{\gamma+\sigma}{2\alpha}} \left\{ C_1 (-1)^{\frac{\gamma}{\alpha}} I\left(\frac{\gamma-\sigma}{\alpha}, \frac{2\sqrt{e^{-\alpha t}\beta\sigma}}{\alpha}\right) \Gamma\left(1 + \frac{\gamma-\sigma}{\alpha}\right) + C_2 (-1)^{\frac{\sigma}{\alpha}} I\left(-\frac{\gamma-\sigma}{\alpha}, \frac{2\sqrt{e^{-\alpha t}\beta\sigma}}{\alpha}\right) \Gamma\left(1 - \frac{\gamma-\sigma}{\alpha}\right) \right\} \quad (9)$$

To determine C_1, C_2 , we use the following boundary conditions: $I_{II}(0) = I_1(t_0)$ and $I'_{II}(0) = I'_1(t_0)$, where the first derivative in region II has the following expression:

$$I'_{II}(0) = \left(\frac{\beta\sigma}{\alpha^2}\right)^{\frac{\gamma+\sigma}{2\alpha}} \left\{ C_1 (-1)^{\frac{\alpha+\gamma}{\alpha}} \Gamma\left(1 + \frac{\gamma-\sigma}{\alpha}\right) \left[\gamma I\left(\frac{\gamma-\sigma}{\alpha}, \frac{2\sqrt{\beta\sigma}}{\alpha}\right) + \sqrt{\beta\sigma} I\left(1 + \frac{\gamma-\sigma}{\alpha}, \frac{2\sqrt{\beta\sigma}}{\alpha}\right) \right] + C_2 (-1)^{\frac{\alpha+\sigma}{\alpha}} \Gamma\left(1 - \frac{\gamma-\sigma}{\alpha}\right) \left[\sigma I\left(-\frac{\gamma-\sigma}{\alpha}, \frac{2\sqrt{\beta\sigma}}{\alpha}\right) + \sqrt{\beta\sigma} I\left(1 - \frac{\gamma-\sigma}{\alpha}, \frac{2\sqrt{\beta\sigma}}{\alpha}\right) \right] \right\} \quad (10)$$

In obtaining the expression above, the following identities were frequently used:^[15,16]

$$\frac{dI(v, x)}{dx} = I(v-1, x) - \frac{v}{x} I(v, x); I(v-1, x) - I(v+1, x) = \frac{2vI(v, x)}{x} \quad (11)$$

After derivations, where the following relation^[16]

$$I(v+1, x)I(-v, x) - I(v, x)I(-v-1, x) = \frac{2\sin(\pi v)}{\pi x} \quad (12)$$

together with $\sin((v \pm 1)\pi) = -\sin(v\pi)$ and the identity relating modified Bessel function of the first and second kind $K(v, x) = \frac{\pi}{2} \frac{I(-v, x) - I(v, x)}{\sin v\pi}$ are used,^[15,16] we finally obtain a surprisingly simple result:

$$I_{II}(t) = I_1(t_0) e^{-\frac{\gamma+\sigma}{2} t} \frac{K\left(\frac{\gamma-\sigma}{\alpha}, \frac{2\sqrt{e^{-\alpha t}\beta\sigma}}{\alpha}\right)}{K\left(\frac{\gamma-\sigma}{\alpha}, \frac{2\sqrt{\beta\sigma}}{\alpha}\right)} \quad (13)$$

where $K(v, x)$ is the modified Bessel function of the second kind.

At maximum and inflection points, $I'_{II} = 0$ and $I''_{II} = 0$, respectively. After extensive simplification of the results, this leads to $(\gamma = R_{0,free} e^{-\alpha t})$, where $R_{0,free} = \beta/\gamma$ is the basic reproduction number in the absence of social distancing:^[6,17]

$$\sqrt{\gamma} K\left(\frac{\gamma-\sigma}{\alpha} + 1, \frac{2\sqrt{\gamma\sigma}}{\alpha} \sqrt{\gamma}\right) = \sqrt{\frac{\gamma}{\sigma}} K\left(\frac{\gamma-\sigma}{\alpha}, \frac{2\sqrt{\gamma\sigma}}{\alpha} \sqrt{\gamma}\right) \quad (14)$$

$$\sqrt{\gamma} K\left(\frac{\gamma-\sigma}{\alpha} + 1, \frac{2\sqrt{\gamma\sigma}}{\alpha} \sqrt{\gamma}\right) = \sqrt{\frac{\gamma}{\sigma}} \left(\frac{\gamma+\sigma}{\sigma}\right) K\left(\frac{\gamma-\sigma}{\alpha}, \frac{2\sqrt{\gamma\sigma}}{\alpha} \sqrt{\gamma}\right) \left(\frac{\gamma}{\sigma} + 1\right) \quad (15)$$

Equations (14) and (15) have to be solved numerically, but, as γ and σ are constants, we, interestingly, obtain that solutions will depend only on α . Since, for the analysis of superlinear and sublinear regimes, only the left inflection point and the maximum are important, we will further omit the second solution of Equation (15) (Equation (14) has one solution), and denote $\gamma_i = f_{i1}(\alpha) \equiv f_i(\alpha)$, $\gamma_m = f_m(\alpha)$ (these two solutions are presented as upper and lower curves on **Figure 2C**, respectively), so that the effective reproduction numbers at inflection and maximum points ($R_{e,i}$ and $R_{e,m}$) are:

$$R_{e,i} \equiv R_{0,free} e^{-\alpha t_i} = f_i(\alpha), \quad R_{e,m} \equiv R_{0,free} e^{-\alpha t_m} = f_m(\alpha). \quad (16)$$

From this follows the length of superlinear regime (between inflection and maximum points):

$$\Delta t \equiv t_m - t_i = \frac{1}{\alpha} \ln\left(\frac{f_i(\alpha)}{f_m(\alpha)}\right) \quad (17)$$

We further Taylor expand $I_{II}(t)$ around the inflection point:

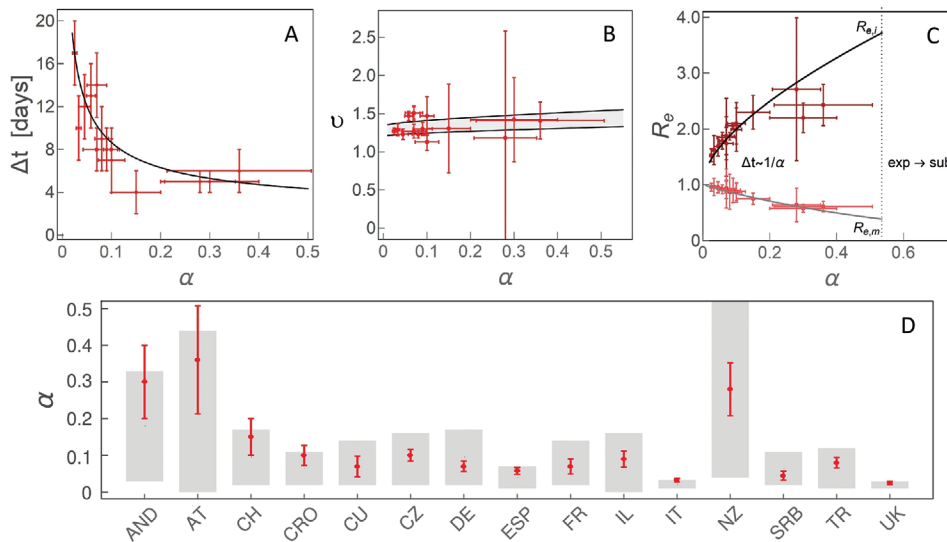


Figure 2. The dependence on the effective social distancing strength (α) of A) Δt , the duration of the superlinear regime, B) ν , the scaling exponent of the superlinear regime, C) $R_{e,i}$, effective reproduction number at the left inflection point ($R_{e,i}$) and the maximum ($R_{e,m}$) of $I(t)$. $\Delta t \approx 1/\alpha$ indicates that the time, in which the change from $R_{e,i}$ to $R_{e,m}$ is exhibited, is approximately inversely proportional to α . “exp \rightarrow sub” indicates the region of α where we predict a direct transition from exponential to sublinear growth. D) Comparison of α constrained from analytical derivations (the grey bands) and numerical analysis, with countries indicated on the horizontal axis by their abbreviations. Results obtained by independent numerical analysis are presented by red dots with corresponding errorbars.

$$I_{II}(t) = I_1(t_0) e^{-\frac{\gamma+\sigma}{2}(t-t_0)} \frac{K\left(\frac{\gamma-\sigma}{\alpha}, \frac{2\sqrt{\gamma\sigma}}{\alpha} \sqrt{f_i(\alpha)}\right)}{K\left(\frac{\gamma-\sigma}{\alpha}, \frac{2\sqrt{\beta\sigma}}{\alpha}\right)} \left[1 - \frac{\gamma\sigma}{\gamma+\sigma}(1-f_i(\alpha))(t-t_0) + \mathcal{O}((t-t_0)^2)\right] \quad (18)$$

In the superlinear regime $D(t) \approx (t-t_s)^\nu$, where ν is the scaling exponent and t_s marks the beginning of this regime. By Taylor expanding $D(t)$ around t_s , using Equations (18) and (3):

$$\nu = 1 + \frac{1}{k\alpha} \frac{\gamma\sigma}{\gamma+\sigma} [f_i(\alpha) - 1] \ln\left(\frac{f_i(\alpha)}{f_m(\alpha)}\right) \quad (19)$$

which is always larger than 1, as expected for the superlinear regime. As t_i is localized toward the beginning of the regime, we estimate $t_i - t_s \approx \frac{\Delta t}{k}$, where $k \approx 3, 4$.

Finally, to provide analytical constrain on α , we Taylor expand $I_{II}(t)$ around the maximum:

$$I_{II}(t) = I_1(t_0) e^{-\frac{\gamma+\sigma}{2}(t-t_0)} \frac{K\left(\frac{\gamma-\sigma}{\alpha}, \frac{2\sqrt{\gamma\sigma}}{\alpha} \sqrt{f_m(\alpha)}\right)}{K\left(\frac{\gamma-\sigma}{\alpha}, \frac{2\sqrt{\beta\sigma}}{\alpha}\right)} \left[1 - \frac{\gamma\sigma}{2}(1-f_m(\alpha))(t-t_m)^2 + \mathcal{O}((t-t_m)^3)\right] \quad (20)$$

As $f_m(\alpha) < 0$, we see that the quadratic term in Equation (20) is always negative, that is, $D(t)$ curve enters sublinear regime around maximum of the infection. By fitting $D(t)$

to $c+d(t-t_m)-f(t-t_m)^3$ in this regime, and by using Equation (20) together with Equation (3), we obtain:

$$\frac{f}{d} = \frac{\gamma\sigma}{6} [1 - f_m(\alpha)] \quad (21)$$

which allows to directly constrain α .

We first numerically analyze outbreak dynamics in the countries that continuously updated^[18] three observable categories (D , A , and F). For a large majority of countries active cases were either not tracked or were not continuously updated, so the analysis is done for ten countries listed in the outline above.

In the exponential regime, the analytical closed-form solution is given by Equation (5). From this, and the initial slope of $\ln(D)$ curve (once the number of counts are out of the stochastic regime), β can be directly determined, while the corresponding eigenvector sets the ratio of I_0 to E_0 . The intercept of the initial exponential growth of D at $t = 0$ sets the product of I_0 and $\varepsilon\delta$. h and m can also be readily constrained, as from Equation (3), they depend only on integrals of the corresponding counts; here note that $d(D-A-F)/dt = hA$. Also,^[17,19,20] $\sigma = 1/3 \text{ day}^{-1}$ and $\gamma = 1/4 \text{ day}^{-1}$, characterize fundamental infectious process, which we assume not to change between different countries.

Only parameters related with the intervention measures ($\alpha, t_0, n, \varepsilon\delta$) are left to be inferred numerically, leading to tightly constrained numerical results. For this, we individually performed joint fit to all three observable quantities (A, D, F) for each country. The errors are estimated through Monte-Carlo^[21,22] simulations, assuming that count numbers follow Poisson distribution.

Representative numerical results are shown in Figure 1 for Germany, while other countries are shown in the Supporting

Information. In Figure 1A–C (and Supporting Information) we see a good agreement of our numerical analysis with all three classes of the case counts. In Figure 1D, we see sharp transitions between the three growth patterns indicated in the figure: i) exponential growth, observed as a straight line in log–linear plot in Figure 1E; ii) superlinear growth, a straight line in log–log plot in Figure 1F; iii) sublinear growth, a straight line in linear–log plot in Figure 1G.

Transition between the growth patterns can be qualitatively understood from Equation (3), and $I(t)$ curve in Figure 1D. The exponential growth has to break after the inflection point of $I(t)$, that is, once the maximum of its first derivative ($I'(t)$ in Figure 1D) is reached. In the superlinear regime, confirmed counts case ($D(t)$) curve is convex ($D''(t) > 0$), so this regime breaks once $I'(t)$ (dashed blue curve) becomes negative. Equivalently, $D(t)$ curve becomes concave (enters sublinear regime) once the maximum of the $I(t)$ is reached. Note that the growth of $D(t)$ can reemerge if the social distancing measures are alleviated. Our model can account for this by allowing transition from protected back to susceptible category, which is out of the scope of this study, but may improve the agreement with the data at later times (see Figure 1A–C). In addition to this numerical/intuitive understanding, we also showed that we analytically reproduce the emergence of these growth regimes (Equations (6), (14), (15)). Can we also analytically derive the parameters that characterize these regimes?

The exponential regime is straightforward to explain, as described above. The superlinear regime is in between the left inflection point and the maximum of $I(t)$, so that infective numbers grow, but with a decreasing rate. While the derivations are straightforward in the exponential regime, they are highly non-trivial during the subsequent subexponential (superlinear and sublinear) growth. As the superlinear regime spans the region between the left inflection point ($t_i, I''(t_i) = 0$) and the maximum ($t_m, I'(t_m) = 0$), its duration is $\Delta t = t_m - t_i$ given by Equation (17), with $\approx 1/\alpha$ dependence, so that weak measures lead to protracted superlinear growth (see Figure 2A). This tendency is also confirmed by independent numerical analysis in Figure 2A, where for each individual country we numerically infer α and extract the length of the superlinear regime. Therefore, the duration of the superlinear regime indicates the effectiveness of introduced social distancing.

The scaling exponent ν of the superlinear regime is given by Equation (19), and shown in Figure 2B, where we predict that all countries are roughly in the same range of $1.2 < \nu < 1.5$ (surprisingly, weakly dependent on α), despite significant differences in the applied measures, demographic and environmental factors. This result is (independently from our model) confirmed from case count numbers (the slope in Figure 1F, and equivalently for other countries, see Figure 2B).

How the effective reproduction number R_e changes during this regime, that is, between the left inflection point and the maximum of $I(t)$? R_e quantifies the average number of secondary cases per infectious case, so that $R_e > 1$ signifies disease outburst, while for $R_e < 1$ the disease starts to be eliminated from the population.^[17] The Equation (16) provides expressions for $R_{e,i}$ (at the inflection point) and $R_{e,m}$ (at the maximum). Interestingly, from Figure 2C, we observe that $R_{e,i}$ and $R_{e,m}$

do not depend on $R_{0,free}$ and are, respectively, significantly larger and smaller than 1, which shows that transition from infection outburst to extinguishing happens during the superlinear growth. Consequently, the steepness of R_e change over the superlinear regime significantly increases (larger change over smaller time interval, see Figure 2C) with the measure strength.

Finally, in the sublinear regime, in a wide vicinity of $I(t)$ maximum (which marks the beginning of the sublinear growth) leading non-linear term of $D(t)$ is cubic ($\approx t^3$, with negative prefactor). This is consistent with the expansion of $I(t)$ around t_m , which has leading negative quadratic (t^2) dependence (see Equations (3) and (20)). The ratio between the prefactors in $D(t)$ expansion is given by Equation (21), from which we see that α can be directly constrained, as shown in Figure 2D. For the ten countries with consistent tracking of D, A , and F , we independently numerically determined α and compared it with analytical results coming from Equation (21), obtaining an excellent agreement between our derivations and numerical results. The obtained α values should be understood as an effective epidemic containment measure—that is, estimating the true result of the introduced measures, which can be used to evaluate the practical effectiveness of the official policies.

To demonstrate how constraining α can aid numerical analysis in the cases when A is not continuously tracked, we next analyze five additional countries listed in the outline above, so that altogether our study covers majority of COVID-19 hotspots, which (at the time of this analysis) are close to saturation in confirmed counts. Furthermore, in the specific cases of UK and Italy, where we analytically obtained both very low and very constrained α ($0.01 < \alpha < 0.04$), we chose five times larger parameter span in α in the numerical analysis, to confirm that these low values are indeed preferred by the exhaustive numerical search. For example, the finally obtained α for Italy (0.033 ± 0.005) and UK (0.025 ± 0.005), together with previously obtained agreements shown in Figure 2A–C, strongly confirm that the observed growth patterns provide invaluable information for successful analysis of the infection progression data.

To further illustrate this, the synergy of analytical derivations and numerical analysis presented above enables us to, directly from the publicly available data, infer key infection parameters necessary to assess epidemics risks (provided in Table S1, Supporting Information). We estimate these parameters by the same model/analysis, for a number of diverse countries, allowing their direct comparison. In **Figure 3**, we show together case fatality rate (CFR), infected fatality rate (IFR) and infection attack rate (AR).^[17,24] CFR is the number of fatalities per confirmed cases. CFR can, in principle, be inferred directly from the data, but since different countries are in different phases of infection, we project forward the number of confirmed cases until a saturation is reached for each country, from which we calculate CFR. IFR (crucial parameter for assessing the risks for infection progression under different scenarios) is the number of fatalities per total number of infected cases, which is a genuine model estimate, due to the unknown total number of infected cases. AR (necessary for understanding the virus recurrence risk) is also determined from our model and provides an estimate of the fraction of the total population that got infected and possibly resistant.

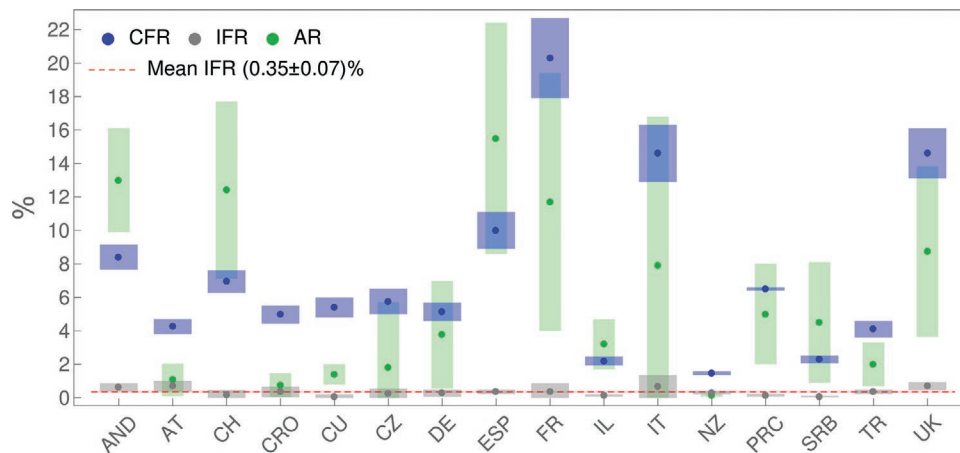


Figure 3. CFR, IFR, and AR, inferred for countries whose abbreviations are indicated on the horizontal axis, are denoted, respectively, by blue, grey, and green dots, with errorbars indicated by corresponding bands. The dashed red horizontal line stands for IFR consistent with a mean value (indicated in the legend). Values for PRC are from ref. [23].

From Figure 3, we see that CFR takes very different values for different countries, from below 2% (New Zealand) to above 20% (France). On the other hand, IFR is consistent with a constant value (the dashed red line in the figure) of $\approx 0.3-0.4\%$. In distinction to IFR, AR also takes diverse values for different countries, ranging from $\approx 1\%$ to as high as $\approx 15\%$ (though with large errorbars). Although diverse, these AR values are well below the classical herd immunity threshold of 60–70%

To summarize, we here developed a novel quantitative framework through which we showed that: i) The emergence of three distinct growth regimes in COVID-19 case counts can be reproduced both analytically and numerically. ii) Typically, a brief superlinear regime is characterized by a sharp transition from outburst to extinguishing the infection, where effective reproduction number changes from much larger to much smaller than one; more effective measures lead to shorter superlinear growth, and to a steeper change of the effective reproduction number. iii) Scaling exponent of the superlinear regime is surprisingly uniform for countries with diverse environmental and demographic factors and epidemics containment policies; this highly non-trivial empirical result is well reproduced by our model. iv) Scaling prefactors in the sublinear regime contain crucial information for analytically constraining infection progression parameters, so that they can be straightforwardly extracted through numerical analysis. Interestingly, we found that the number of COVID-19 fatalities per total number of infected is highly uniform across diverse analyzed countries, in distinction to other (highly variable) infection parameters, and about twice higher than commonly quoted for influenza (0.3–0.4% compared to 0.1–0.2%), which may be valuable for direct assessment of the epidemics risks.

While state-of-the-art approach in epidemiological modeling uses computationally highly demanding numerical simulations, the results above demonstrate a shift of paradigm toward simpler, but analytically tractable models, that can both explain common dynamical features of the system and be used for straightforward and highly constrained parameter inference. This shift is based on a novel framework that relates universal growth patterns with characteristic points of the infective curve, followed by analytical derivations in the vicinity of these points, in an approach akin to those in a number of

physics problems. The framework presented here can be, in principle, further extended toward, for example, including stochastic effects or different heterogeneities such as age-structure. However, these are non-trivial tasks, and it remains to be seen to what extent the analytical results can be obtained in those more complex models. Overall, as our approach does not depend on any COVID-19 specifics, the developed framework can also be readily applied to potential outbursts of future infections.

Supporting Information

Supporting Information is available from the Wiley Online Library or from the author.

Acknowledgements

This work was supported by the Ministry of Education, Science and Technological Development of the Republic of Serbia.

Conflict of Interest

The authors declare no conflict of interest.

Data Availability Statement

The data used in this study are openly available in Worldometer at <https://www.worldometers.info/coronavirus/>, reference number [7]. Parameters inferred through the analysis are available in the supplementary material of this article.

Keywords

dynamical growth patterns, infections disease modeling, physics and society, scaling of epidemics growth

Received: October 8, 2020
Revised: January 16, 2021
Published online: March 1, 2021

- [1] WHO report. <https://www.who.int/emergencies/diseases/novel-coronavirus-2019/situation>.
- [2] O. Diekmann, H. Heesterbeek, T. Britton, *Mathematical Tools for Understanding Infectious Disease Dynamics*, Princeton University Press, Princeton, NJ **2012**.
- [3] M. Martcheva, *An Introduction to Mathematical Epidemiology*, Springer, Berlin **2015**.
- [4] M. J. Keeling, P. Rohani, *Modeling Infectious Diseases in Humans and Animals*, Princeton University Press, Princeton, NJ **2011**.
- [5] H. Tian, Y. Liu, Y. Li, C. H. Wu, B. Chen, U. G. Kraemer, B. Li, J. Cai, B. Xu, Q. Yang, B. Wang, P. Yang, Y. Cui, Y. Song, P. Zheng, Q. Wang, O. N. Bjornstad, R. Yang, B. T. Grenfell, O. G. Pybus, C. Dye, *Science* **2020**, 368, 638.
- [6] G. Chowell, L. Sattenspiel, S. Bansal, C. Viboud, *Physics of Life Reviews* **2016**, 18, 66.
- [7] Worldometer **2020**. COVID-19 Coronavirus Pandemic. <https://www.worldometers.info/coronavirus/> (accessed: June 2020).
- [8] M. Day, *BMJ: British Medical Journal* **2020**, 368, m1165.
- [9] G. N. Wong, Z. J. Weiner, A. V. Tkachenko, A. Elbanna, S. Maslov, N. Goldenfeld, *arXiv:200602036*, **2020**.
- [10] J. R. Dormand, P. J. Prince, *J. Comput. Appl. Math.* **1980**, 6, 19.
- [11] J. M. Vilar, L. Saiz. medRxiv 2020.11.26.20239434, **2020**.
- [12] N. C. Grassly, C. Fraser, *Nat. Rev. Microbiol.* **2008**, 6, 477.
- [13] R. Phillips, J. Kondev, J. Theriot, H. Garcia, *Physical Biology of the Cell*, Garland Science, New York, NY **2012**.
- [14] F. Bowman, *Introduction to Bessel Functions*, Dover Publications, New York, NY **1958**.
- [15] D. Zwillinger, *Standard Mathematical Tables and Formulae*, CRC Press, Boca Raton, FL **1995**.
- [16] M. Abramowitz, T. A. Stegun, *Handbook of Mathematical Functions* (Ed: M. Abramowitz), Dover Publications, New York, NY **1972**.
- [17] Y. M. Bar-On, A. I. Flamholz, R. Phillips, R. Milo, *eLife* **2020**, 9, e57309.
- [18] E. Dong, H. Du, L. Gardner, *Lancet Infect. Dis.* **2020**, 20, 533.
- [19] R. Li, S. Pei, B. Chen, Y. Song, T. Zhang, W. Yang, J. Shaman, *Science* **2020**, 368, 489.
- [20] X. He, E. H. Y. Lau, P. Wu, X. Deng, J. Wang, X. Hao, Y. C. Lau, J. Y. Wong, Y. Guan, X. Tan, X. Mo, Y. Chen, B. Liao, W. Chen, F. Hu, Q. Zhang, M. Zhong, Y. Wu, L. Zhao, F. Zhang, B. J. Cowling, F. Li, G. M. Leung, *Nat. Med.* **2020**, 26, 672.
- [21] W. H. Press, B. P. Flannery, S. A. Teukolsky, W. T. Vetterling, *Numerical Recipes: The Art of Scientific Computing*, Cambridge University Press, Cambridge **1986**.
- [22] R. W. Cunningham, *Comput. Phys.* **1993**, 7, 570.
- [23] M. Djordjevic, M. Djordjevic, I. Salom, A. Rodic, D. Zigic, O. Milicevic, B. Ilic, *arXiv:2005.09630*, **2020**.
- [24] S. Eubank, I. Eckstrand, B. Lewis, S. Venkatramanan, M. Marathe, C. L. Barrett, *Bull. Math. Biol.* **2020**, 82, 1.
- [25] T. Britton, F. Ball, P. Trapman, *arXiv:2005.03085*, **2020**.
- [26] F. P. Havers, C. Reed, T. Lim, J. M. Montgomery, J. D. Klena, A. J. Hall, A. M. Fry, D. L. Cannon, C.-F. Chiang, A. Gibbons, I. Krapiunaya, M. Morales-Betoulle, K. Roguski, M. Ata Ur Rasheed, B. Freeman, S. Lester, L. Mills, D. S. Carroll, S. M. Owen, J. A. Johnson, V. Semenova, C. Blackmore, D. Blog, S. J. Chai, A. Dunn, J. Hand, S. Jain, S. Lindquist, R. Lynfield, S. Pritchard, et al., *JAMA Intern. Med.* **2020**, 180, 1576.

PRESENTATIONS

A. Contributed talks at conferences and workshops

1. Stefan Stojku, Marko Djordjevic, Pasi Huovinen, Magdalena Djordjevic, *Shape of the quark-gluon plasma droplet reflected in the high- p_{\perp} data*, Zimanyi school 2019: 19th Zimanyi school - Winter workshop on heavy ion physics, December 2019, Budapest, Hungary

ZIMÁNYI SCHOOL 2019



Gyórfi András: Az úton (On the road)

**19th ZIMÁNYI SCHOOL
WINTER WORKSHOP
ON HEAVY ION PHYSICS**


December 2-6, 2019

Budapest, Hungary



József Zimányi (1931 - 2006)

Speakers: Mark Strikman (Pennsylvania State University (US)), Mark Strikman (Penn State University)


 buda.pdf

10:00

Hadron fragmentation in the non-extensive statistical approach

🕒 25m

Speakers: Gergely Barnafoldi (Hungarian Academy of Sciences (HU)), Gergely Barnafoldi (Hungarian Academy of Sciences (HU)), Dr Gergely Gabor Barnafoldi (Wigner RCP Hungarian Academy of Sciences (HU))

 BarnafoldiGG_Zima...

10:25 – 10:55 **Coffee break**

📍 Bldg 3, Council room

10:55 – 12:40 **Jets (section chair: M. Strikman)**


📍 Bldg 3, Council room

10:55

Latest Results from RHIC and BNL

🕒 30m

Speaker: Michael Tannenbaum (Brookhaven National Laboratory (US))


 rTannenbaum-Zima...

11:25

Dynamical jet energy loss

🕒 25m

Speaker: Magdalena Djordjevic (Institute of Physics Belgrade)


 ZimanyiSchool_MDj...

11:50

Beyond the soft-gluon approximation in calculating hard probe radiative energy loss

🕒 20m

Speaker: Dr Bojana Ilic (Blagojevic) (Institute of Physics Belgrade)


 Zimanyi19_Bojana_I...

12:10

DREENA framework as a multipurpose tool for QGP tomography

🕒 15m

Speaker: Dusan Zigic (Institute of Physics Belgrade)


 ZimanyiSchool19_D...

12:25

Shape of the quark gluon plasma droplet reflected in the high pt data

🕒 15m

Speaker: Stefan Stojku (Institute of Physics University of Belgrade)

 ZimanyiSchool2019...

2. Stefan Stojku, Marko Djordjevic, Pasi Huovinen, Magdalena Djordjevic, *From high- p_{\perp} theory and data to inferring the anisotropy of quark-gluon plasma*, Frontiers in Nuclear and Hadronic Physics 2020, Florence, Italy

School

Frontiers in Nuclear and Hadronic Physics 2020

Feb 24, 2020 - Mar 06, 2020

Student Seminars

Session 1 - Thursday, February 27th, 11:15 - 13:15

11:15 - 11:35	Stefan Stojku <i>Shape of the quark gluon plasma droplet reflected in the high p_t data</i>
11:35 - 11:55	Mohsen Haddadi Moghaddam <i>Accelerating longitudinal expansion of resistive relativistic-magneto-hydrodynamic in heavy ion collisions</i>
11:55 - 12:15	Junhong Liu <i>Diffusion of heavy quarks in the early stage of high energy nuclear collisions at RHIC and LHC</i>
12:15 - 12:35	Rajeev Singh <i>Spin Hydrodynamics for the description of polarization of Lambda hyperons</i>
12:35 - 12:55	Michal Barej <i>Wounded quarks in heavy-ion collisions</i>

3. Stefan Stojku, Jussi Auvinen, Marko Djordjevic, Pasi Huovinen, Magdalena Djordjevic, *QGP tomography: inferring bulk medium properties from high- p_{\perp} data*, Zimanyi school 2020: 20th Zimanyi school - Winter workshop on heavy ion physics, December 2020, Budapest, Hungary

ZIMÁNYI SCHOOL 2020



J. E.: From darkness, the light

20th ZIMÁNYI SCHOOL

WINTER WORKSHOP

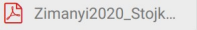
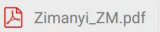
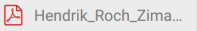
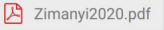
ON HEAVY ION PHYSICS

December 7-11, 2020

Budapest, Hungary



József Zimányi (1931 - 2006)

THURSDAY, 10 DECEMBER		
08:00	→ 09:45	Flow and heavy flavours (section chair: Panos Christakoglou)
08:00	QGP tomography: inferring bulk medium properties from high pt data	🕒 15m
	Speaker: Stefan Stojku (Institute of Physics University of Belgrade)	
		
08:15	Investigation of anisotropic flow in large and small collision systems with ALICE	🕒 15m
	Speakers: Zuzana Moravcova (University of Copenhagen (DK)), Zuzana Moravcová (Czech Technical University in Prague)	
		
08:30	Fluctuations of anisotropic flow in transport	🕒 15m
	Speaker: Hendrik Roch (University Bielefeld)	
		
08:45	Probing pt-dependent flow vector fluctuations	🕒 15m
	Speaker: Emil Gorm Nielsen (University of Copenhagen (DK))	
		
09:00	Heavy-flavour production in proton-proton collisions with the ALICE experiment	🕒 15m
	Speaker: Laszlo Gyulai (Wigner Research Centre for Physics (Wigner RCP) (HU))	

4. Stefan Stojku, Jussi Auvinen, Marko Djordjevic, Pasi Huovinen, Magdalena Djordjevic, *Thermalization time constrained by high- p_{\perp} QGP tomography*, Online Strangeness in Quark Matter Conference 2021, May 2021

The screenshot shows the interface for the 19th International Conference on Strangeness in Quark Matter (SQM2021), held online from May 17-22, 2021. The header features the conference title, dates, and location (Brookhaven National Laboratory, Upton, New York). The main banner includes the SQM2021 logo, a sun icon, and the Statue of Liberty. Below the banner, the date '17-22 May 2021' and a search bar are visible. The left sidebar contains navigation links: Overview, Scientific program, ZOOM connection, Call for Abstracts, Timetable, Contribution List (highlighted), Registration, Participant List, Important dates, Announcements, Committees, Code of conduct, and Proceedings. The main content area displays the title 'Thermalization time constrained by high-pt QGP tomography' with a 'Theory talk' tag and a 'Bulk (Small systems)' category. It lists the speaker as Mr. Stefan Stojku and provides a detailed description of the research, mentioning the use of the DREENA-A formalism and 2+1 dimensional hydrodynamical simulations. The primary authors listed are Mr. Stefan Stojku, Dr. Jussi Auvinen, Prof. Marko Djordjevic, and Dr. Pasi Huovinen.

5. Stefan Stojku, Jussi Auvinen, Marko Djordjevic, Pasi Huovinen, Magdalena Djordjevic, *Anisotropy of quark-gluon plasma inferred from high- p_{\perp} data*, Workshop of the Network NA7-Hf-QGP of the European program 'STRONG-2020' and the HFHF, October 2021, Hersonissos, Crete, Greece



- 11:30 – 11:55 **Gábor Balassa** (*Wigner Research Centre for Physics, Budapest*)
'Estimating tetraquark cross-sections from a statistical model'
- 11:55 – 12:20 **Anna Schäfer** (*GU, Frankfurt*)
'Exploring the high baryon-density regime of the QCD phase diagram within a novel hybrid model'
- 12:20 – 12:45 **Antoine Pfaff** (*SUBATECH, Nantes*)
'A bayesian analysis of hybrid star properties with the NJL model'
- 12:45 – 13:10 **Johannes Roth** (*Giessen Uni.*)
'Real-time methods for spectral functions'

13:30 – 14:30 *Lunch*

- 17:00 – 17:25 **Stefan Stojku** (*Institute of Physics, University of Belgrade*)
'Anisotropy of quark-gluon plasma inferred from high-pt data'
- 17:25 – 17:50 **Andrea Palermo** (*Università di Firenze, INFN Firenze*)
'Polarization as a signature of local parity violation in hot QCD matter'
- 17:50 – 18:15 **Christian Kummer** (*Giessen Uni.*)
'Pions in GiBUU simulations at lower energies'
- 18:15 - 18:25 *Break*
- 18:25 – 18:50 **Leon Sieke** (*Giessen Uni.*)
'Real-time methods for spectral functions'
- 18:50 – 19:15 **Oleksii Ivanytskyi** (*Uni. of Wroclaw*)
'Relativistic density functional approach to unified description of quark-hadron matter'

8 October, Friday

- 9:30 – 10:20 **David Blaschke** (*Uni. of Wroclaw*)

B. Contributed posters at conferences and workshops

1. Stefan Stojku, Magdalena Djordjevic, *From R_{AA} to energy loss temperature proportionality factor*, Strangeness in Quark Matter, Jun 2019, Bari, Italy

The 18th International Conference on
Strangeness in Quark Matter
10-15 June 2019, Bari (Italy)

STRANGENESS IN QUARK MATTER
Bari
2019

© Foto: Pia Bole / wikipedia / License: Creative Commons CC-by-sa-3.0 de

Europa Zürich online

Overview
SQM 2019 main website
Timetable
Overall layout
Call for Abstracts
Contribution List
Book of Abstracts
Registration
Fee payment
Participant List
Conference info
✉ sqm2019@ba.infn.it

From R_{AA} to energy loss temperature proportionality factor

11 Jun 2019, 18:45
2h
Sala B1+C1 (Giulia Center) (Villa Romanazzi Carducci)

Poster Poster session with "a..."

Speaker
Stefan Stojku (Institute of Physics ...)

Description


When traversing QCD medium, high p_{\perp} partons lose energy, which is measured by suppression, and also predicted by various energy loss models. A crucial test of different energy loss mechanisms is their dependence on the medium temperature. Though it is commonly assumed that this dependence is cubic, different effects such as Debye screenings, finite parton masses, infrared cutoffs, etc., modify it differently for different energy losses models. Therefore, providing a theoretical procedure which is able to extract this temperature proportionality factor directly from the suppression data, would enable both differentiating between different energy loss models and gaining better understanding of parton-QGP interactions. In this work [1], we propose a method (based on our recently developed DREENA framework [2]) to infer the energy loss temperature dependence from high p_{\perp} suppression, and demonstrate that our procedure presents a reliable tool for such a purpose.

[1] S. Stojku, et al., in preparation (2019).
[2] D. Zigic, I. Salom, J. Auvinen, M. Djordjevic and M. Djordjevic, Phys. Lett. B (in press, 2019); arXiv:1805.03494.

Track Heavy Flavour

Primary author
Stefan Stojku (Institute of Physics ...)

2. [Stefan Stojku](#), Jussi Auvinen, Marko Djordjevic, Pasi Huovinen, Magdalena Djordjevic, *QGP tomography: inferring bulk medium properties from high- p_{\perp} data*, Initial Stages 2021, January 2021, Weizmann Institute of Science, Israel



IS2021
The VIth International Conference on the
INITIAL STAGES
OF HIGH-ENERGY NUCLEAR
COLLISIONS

Initial Stages 2021

10–15 Jan 2021
Weizmann Institute of Science
Asia/Jerusalem timezone

Enter your search term

See you at IS2023 in Copenhagen in June 2023

Overview

Scientific Programme

Call for Abstracts

Book of Abstracts

Timetable

Contribution List

Registration

Participant List

Program and local organizing committee

International Advisory Committee

Important dates

Previous Stages

Sponsors

Contact

initial_stages.2021@gm...

Thermalization time constrained by high-pt QGP tomography

📅 12 Jan 2021, 19:40

🕒 1h 30m

📍 Patio (vDLCC)

[bullet talk \(poster\)](#) [The initial stages of ...](#) [Poster](#)

Speaker

👤 [Mr Stefan Stojku](#) (Institute of Physics ...)

Description

We show that high- p_{\perp} R_{AA} and v_2 are way more sensitive to the QGP thermalization time, τ_0 , than the distributions of low- p_{\perp} particles, and that the high- p_{\perp} observables prefer relatively late thermalization at $\tau_0 \sim 1$ fm/c. To calculate high- p_{\perp} R_{AA} and v_2 , we employ our newly developed DREEN-A formalism, which combines state-of-the-art dynamical energy loss model with 3+1-dimensional hydrodynamical simulations. The model applies to both light and heavy flavor, and we predict a larger sensitivity of heavy observables to the thermalization time. Elliptic flow parameter v_2 is also more sensitive to τ_0 than R_{AA} due to non-trivial differences in the evolution of in-plane and out-of-plane temperature profiles. This presents the first time when a parameter describing bulk QGP has been constrained by high- p_{\perp} observables and related theory, i.e., by so-called QGP tomography.

Primary authors

👤 [Mr Stefan Stojku](#) (Institute of Physics ...)

👤 [Dr Jussi Auvinen](#) (Institute of Physics ...)

👤 [Prof. Marko Djordjevic](#) (University of Belgra ...)

👤 [Dr Pasi Huovinen](#) (Institute of Physics ...)

👤 [Magdalena Djordjevic](#) (Institute of Physics ...)



Република Србија
Универзитет у Београду
Физички факултет
Д.Бр.2019/8002
Датум: 17.12.2021. године

На основу члана 161 Закона о општем управном поступку и службене евиденције издаје се

УВЕРЕЊЕ

Стојку (Дорел) Стефан, бр. индекса 2019/8002, рођен 15.04.1994. године, Панчево, Република Србија, уписан школске 2021/2022. године, у статусу: финансирање из буџета; тип студија: докторске академске студије; студијски програм: Физика.

Према Статуту факултета студије трају (број година): три.
Рок за завршетак студија: у двоструком трајању студија.

Ово се уверење може употребити за регулисање војне обавезе, издавање визе, права на дечији додатак, породичне пензије, инвалидског додатка, добијања здравствене књижице, легитимације за повлашћену возњу и стипендије.

Овлашћено лице факултета



[Handwritten signature]



Република Србија
Универзитет у Београду
Физички факултет
Д.Бр.2019/8002
Датум: 17.12.2021. године

На основу члана 161 Закона о општем управном поступку и службене евиденције издаје се

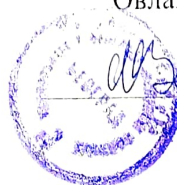
УВЕРЕЊЕ

Стојку (Дорел) Стефан, бр. индекса 2019/8002, рођен 15.04.1994. године, Панчево, Република Србија, уписан школске 2021/2022. године, у статусу: финансирање из буџета; тип студија: докторске академске студије; студијски програм: Физика.

Према Статуту факултета студије трају (број година): три.
Рок за завршетак студија: у двоструком трајању студија.

Ово се уверење може употребити за регулисање војне обавезе, издавање визе, права на дечији додатак, породичне пензије, инвалидског додатка, добијања здравствене књижице, легитимације за повлашћену возњу и стипендије.

Овлашћено лице факултета



[Handwritten signature]



Република Србија
Универзитет у Београду
Физички факултет
Број индекса: 2019/8002
Датум: 17.12.2021.

На основу члана 29. Закона о општем управном поступку и службене евиденције издаје се

УВЕРЕЊЕ О ПОЛОЖЕНИМ ИСПИТИМА

Стефан Стојку, име једног родитеља Дорел, рођен 15.04.1994. године, Панчево, Република Србија, уписан школске 2019/2020. године на докторске академске студије, школске 2021/2022. године уписан на статус финансирање из буџета, студијски програм Физика, током студија положио је испите из следећих предмета:

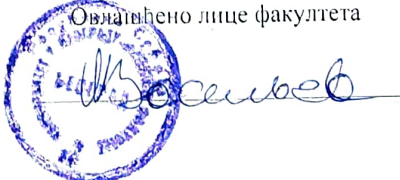
Р.бр.	Шифра	Назив предмета	Оцена	ЕСПБ	Фонд часова**	Датум
1.	ДС15ВО2	Монте Карло симулације у физици	10 (десет)	15	I:(8+0+0)	18.09.2020.
2.	ДС15ТНФ	Теоријска нуклеарна физика	10 (десет)	15	II:(8+0+0)	25.09.2020.
3.	ДС15ФРНД1	Рад на докторату 1. део	П.	30	I:(0+0+12) II:(0+0+12)	
4.	ДС15НФ7	Анализа података у физици високих енергија	10 (десет)	15	III:(8+0+0)	13.07.2021.
5.	ДС15ФРНД2	Рад на докторату 2. део	П.	30	III:(0+0+12) IV:(0+0+12)	
6.	ДС15НФ6	Феноменологија у физици честица	10 (десет)	15	III:(8+0+0)	24.09.2021.

* - еквивалентиран/признат испит.

** - Фонд часова је у формату (предавања+вежбе+остало).

Општи успех: 10,00 (десет и 00/100), по годинама студија (10,00, 10,00, /).

Овлашћено лице факултета





Република Србија
Универзитет у Београду

Оснивач: Република Србија

Дозволу за рад број 612-00-02666/2010-04 од 12. октобра 2011.
године је издало Министарство просвете и науке Републике Србије

Физички факултет, Београд

Оснивач: Република Србија

Дозволу за рад број 612-00-02409/2014-04 од 8. септембра 2014. године је издало
Министарство просвете, науке и технолошког развоја Републике Србије

УБ



Диплома

Стефан, Дорел, Стојку

рођен 15. априла 1994. године, Панчево, Република Србија, уписан школске 2012/2013.

године, а дана 27. фебруара 2018. године завршио је основне академске студије, првог

степена, на студијском програму Теоријска и експериментална физика, обима

240 (двеста четрдесет) бодова ЕСПБ са просечном оценом 9,82 (девет и 82/100).

На основу тога издаје му се ова диплома о стеченом високом образовању и стручном називу

дипломирани физичар

Број: 11400100

У Београду, 1. децембра 2020. године

Декан

Проф. др Иван Белча

Ректор

Проф. др Иванка Појовић

00114297



Република Србија
Универзитет у Београду

Оснивач: Република Србија

Дозволу за рад број 612-00-02666/2010-04 од 12. октобра 2011.
године је издало Министарство просвете и науке Републике Србије

Физички факултет, Београд

Оснивач: Република Србија

Дозволу за рад број 612-00-02409/2014-04 од 8. септембра 2014. године је издало
Министарство просвете, науке и технолошког развоја Републике Србије

УБ



Диплома

Стефан, Дорел, Стојку

рођен 15. априла 1994. године, Панчево, Република Србија, уписан школске
2018/2019. године, а дана 10. јула 2019. године завршио је мастер академске студије,
групе степенa, на студијском програму Теоријска и експериментална физика,
обима 60 (шездесет) бодова ЕСПБ са просечном оценом 9,67 (девет и 67/100).

На основу тога издаје му се ова диплома о стеченом високом образовању и академском називу
мастер физичар

Број: 11100800

У Београду, 30. септембра 2020. године

Декан
Проф. др Иван Белча

Ректор
Проф. др Иванка Појовић

00111177



ДОКТОРСКЕ
СТУДИЈЕ

ПРЕДЛОГ ТЕМЕ ДОКТОРСКЕ ДИСЕРТАЦИЈЕ
КОЛЕГИЈУМУ ДОКТОРСКИХ СТУДИЈА

Школска година
2021/2022

Подаци о студенту

Име

Стефан

Презиме

Стојку

Број индекса

8002/2019

Научна област дисертације

Физика високих енергија и
нуклеарна физика

Подаци о ментору докторске дисертације

Име

Магдалена

Презиме

Ђорђевић

Научна област

Звање

Научни саветник

Институција

Институт за физику

Предлог теме докторске дисертације

Наслов

Properties of quark-gluon plasma inferred from high- p_T data
Сређивање особина кварк-глуонске плазме на основу
високоенергијских честица

Уз пријаву теме докторске дисертације Колегијуму докторских студија,
потребно је приложити следећа документа:

1. Семинарски рад (дужине до 10 страница)
2. Кратку стручну биографију писану у трећем лицу јединине
3. Фотокопију индекса са докторских студија

Датум 16. 11 2021.

Потпис ментора Јарден Ђ.

Потпис студента Стефан Ђукић

Мишљење Колегијума докторских студија

Након образложења теме докторске дисертације Колегијум докторских студија је тему

прихватио

није прихватио

Датум 01. 12. 2021

Продекан за науку Физичког факултета

Стефан Ђукић